Available online at www.sciencedirect.com
SCIENCE DIRECT®
ELSEVIER
Physica D 182 (2003) 151–178
PHYSICA D
www.elsevier.com/locate/physd

Phase space structure of multi-dimensional systems by means of the mean exponential growth factor of nearby orbits

P.M. Cincotta [a,*], C.M. Giordano [a], C. Simó [b]

[a] *Facultad de Ciencias Astronómicas y Geofísicas, Universidad Nacional de La Plata, Paseo del Bosque, 1900 La Plata, Argentina*
[b] *Departament de Matemàtica Aplicada i Anàlisi, Universitat de Barcelona, Gran Via 585, 08007 Barcelona, Spain*

Received 1 March 2002; received in revised form 26 September 2002; accepted 10 December 2002
Communicated by I. Mezic

Abstract

In this paper we deal with an alternative technique to study global dynamics in Hamiltonian systems, *the mean exponential growth factor of nearby orbits* (MEGNO), that proves to be efficient to investigate both regular and stochastic components of phase space. It provides a clear picture of resonance structures, location of stable and unstable periodic orbits as well as a measure of hyperbolicity in chaotic domains which coincides with that given by the Lyapunov characteristic number. Here the MEGNO is applied to a rather simple model, the 3D perturbed quartic oscillator, in order to visualize the structure of its phase space and obtain a quite clear picture of its resonance structure. Examples of application to multi-dimensional canonical maps are also included.

Keywords: Global dynamics; Detection of chaos; Lyapunov characteristic number

1. Introduction

A combination of analytic, geometric and topological tools is required in order to get a detailed account of the local dynamics around some well-known objects (such as fixed points, periodic or quasi-periodic orbits, invariant manifolds, etc.) and the bifurcations that occur when changing parameters. Meanwhile, more global problems, concerning either a big part of the phase space or a large set of the parameter space, require of probabilistic methods and computing several numerical indicators. But, whenever a detailed knowledge of the dynamics in a large set is looked for, we can either extend the local analysis to larger domains, say by using normal forms up to a relatively large order and unfold the bifurcations found or perform systematic numerical experiments, such as the computation of invariant objects and, later on, to continue them with respect to parameters and so detect the bifurcations. This has been the approach used in recent papers such as [1,4], following a methodology presented in [3]. Both approaches, however, demand a considerable computational effort, which points out the convenience of

* Corresponding author.
E-mail addresses: pmc@fcaglp.fcaglp.unlp.edu.ar (P.M. Cincotta), giordano@fcaglp.fcaglp.unlp.edu.ar (C.M. Giordano), carles@maia.ub.es (C. Simó).

0167-2789/$ – see front matter © 2003 Elsevier B.V. All rights reserved.
doi:10.1016/S0167-2789(03)00103-9

having some fast indicators aiming at a significant knowledge of the dynamics in a fairly quick way (see [25] and references therein). Such a numerical tool is sketched herein which succeeds in providing detailed indications of the global dynamics in relatively short motion times.

In fact, few tools prove to be useful when studying global dynamics in Hamiltonian systems or maps. In those cases of divided phase space, which are the most, different techniques are required depending on whether the structure of the regular or stochastic component is to be investigated. For instance, a Fourier technique such as (Laskar) frequency map analysis (FMA) [19–21], is a powerful tool, provided that the phase space is almost completely foliated by invariant tori, since it allows a very precise determination of the frequencies associated to the KAM tori, thus furnishing information about the orbital structure of the system. A detailed discussion on the refined Fourier analysis, which is the basis of the FMA, including a thorough study of the error estimates can be found in [12], where also several examples related to the ones in this paper have been included. However, when irregular motion occupies a large fraction of the phase space, the FMA is no longer that useful, since, though a linear diffusion-like coefficient in frequency space may be derived, it is not quite clear whether this coefficient does provide a good measure of chaos.

For irregular, stochastic regions of phase space, the largest Lyapunov characteristic number (LCN), or maximal Lyapunov exponent, gives a direct measure of hyperbolicity, being the latter the underlying structure of chaotic domains (see [11]). But, though the LCN is a good indicator of the stability of the motion from a theoretical point of view, the motion time required to get a relatively good estimation of its value used to be rather large. Moreover, since the relative error gets larger as the LCN gets smaller, the computed value for moderate times is rather far from the actual value in case of regular motion, leading to an erroneous identification of the orbit. In sum, for comparatively short motion times, the LCN is certainly not an adequate indicator. On the other hand, the motion times needed for a fair estimation of the LCN are too long when dealing with large ensembles ($\gtrsim 10^4$ orbits in the case of flows and $\gtrsim 10^6$ orbits in the case of maps), which, however, cannot be a problem if large arrays of processors are available.

The use of *fast Lyapunov indicators* (FLI) has been recently popularized (see [9,10]). Indeed, to decide about the regular or chaotic behavior of some orbit, you can just follow the evolution of the length of a vector transported by the variational flow (or by the differential of the map in the case of discrete dynamical systems). If such a length increases by a factor less than some threshold L during a time span T, we consider the motion as regular. Otherwise, if a factor L is reached before T, we consider it as chaotic. The point is the proper choice of both L and T. Large values of T imply large computational time, while small values of T, depending on L, have the risk of considering as chaotic motion which is actually regular or vice versa. This fact already pointed out in [12] will be discussed below.

Here we address a new technique, *the mean exponential growth factor of nearby orbits* (MEGNO)—described in detail in [7]—that provides an alternative tool to explore the phase space, allowing to consider shorter motion times. This efficient tool is not only suitable to investigate both regular and stochastic components of the phase space, but also produces in addition a good estimation of the LCN. The MEGNO is a global indicator of the dynamics as well as it is capable to detect high-order resonances. Actually, its ability to reveal the fine structure of the phase space is due to its sensitivity to the presence of unstable periodic orbits, the very origin of chaos. The required computational effort is almost the same needed to compute the LCN. It requires the integration of both the field equations and the concomitant first variationals, but over much shorter time intervals, since it takes due advantage of all the dynamical information that there remains hidden along the orbit and its tangent vector.

The fact that the MEGNO is able to provide good indications of the local hyperbolic properties of an orbit in short time intervals has a side effect. Indeed, the LCN is constant on a connected component of the stochastic set. Hence, it gives an average indication of the hyperbolicity on this component. This average does not discriminate whether the orbit has spent large intervals of time close to some invariant torus for instance. It is known that invariant tori are quite *sticky* and, for some time interval, motion close to them displays only, at most, a mild stochasticity. Hence, it

is far more instructive to look at global dynamical properties by means of a large ensemble of data, each one telling about local properties around it.

A different method to evaluate the LCN is presented in [2] but there the dynamics is quite special, being typically the superposition of an exponentially increasing function and large quasi-periodic oscillations.

The present effort is devoted to show how a rather simple technique, the MEGNO, succeeds in providing detailed indications on the global dynamics of multi-dimensional Hamiltonian systems and maps. Below, we summarize the MEGNO technique and illustrate its performance in the well-known 2D Hénon–Heiles model. Then we apply it to a rather simple 3D model, the perturbed 3D quartic oscillator, in order to visualize the structure of its phase space. Next we present a generalized version of the MEGNO and apply it to a 2D and a 4D area-preserving maps. Some comparisons with the FMA and FLI are included. The presentation is made in the context of conservative systems, despite the fact that the domain of applicability is general.

We would like to point out that the MEGNO has recently been successfully applied to astronomical problems (see [13–15]). An application providing numerical evidence for theoretical conjectures in ergodic theory can be found in [22].

2. The MEGNO

Let $H(\boldsymbol{p}, \boldsymbol{q})$ with $\boldsymbol{p}, \boldsymbol{q} \in \mathbb{R}^N$ denote an N-dimensional Hamiltonian, assumed to be autonomous just for the sake of simplicity since this is actually not required for the present formulation. On introducing the notation $\boldsymbol{x} = (\boldsymbol{p}, \boldsymbol{q}) \in \mathbb{R}^{2N}$, $\boldsymbol{v} = (-\partial H/\partial \boldsymbol{q}, \partial H/\partial \boldsymbol{p}) \in \mathbb{R}^{2N}$, the equations of motion read:

$$\dot{\boldsymbol{x}} = \boldsymbol{v}(\boldsymbol{x}). \tag{1}$$

Let $\gamma(t)$ be an arc of an orbit of flow (1) on a compact energy surface $M_h \subset \mathbb{R}^{2N}$, $M_h = \{\boldsymbol{x} : H(\boldsymbol{p}, \boldsymbol{q}) = h\}$, so that

$$\gamma(t) = \{\boldsymbol{x}(t'; \boldsymbol{x}_0) : \boldsymbol{x}_0 \in M_h, 0 \le t' < t\} \tag{2}$$

and the full positive orbit is $\gamma = \lim_{t\to\infty} \gamma(t)$.

Relevant information about the flow in the vicinity of any orbit γ is gained through its largest LCN, $\sigma(\gamma)$, defined as

$$\sigma(\gamma) = \lim_{t\to\infty} \sigma_1(\gamma(t)), \qquad \sigma_1(\gamma(t)) = \frac{1}{t} \ln \frac{\|\boldsymbol{\delta}(\gamma(t))\|}{\|\boldsymbol{\delta}_0\|} \tag{3}$$

with $\boldsymbol{\delta}(\gamma(t))$ and $\boldsymbol{\delta}_0$ "infinitesimal displacements" from γ at times t and 0, respectively (see below) and where $\|\cdot\|$ is some norm. The fact that the LCN measures the "mean exponential rate of divergence of nearby orbits", is stated explicitly when recasting (3) in the integral form:

$$\sigma(\gamma) = \lim_{t\to\infty} \frac{1}{t} \int_0^t \frac{\dot{\delta}(\gamma(t'))}{\delta(\gamma(t'))}\, \mathrm{d}t' = \overline{\left(\frac{\dot{\delta}}{\delta}\right)} \tag{4}$$

with $\delta \equiv \|\boldsymbol{\delta}\|$, $\dot{\delta} \equiv \mathrm{d}\delta/\mathrm{d}t = \dot{\boldsymbol{\delta}} \cdot \boldsymbol{\delta}/\|\boldsymbol{\delta}\|$, the bar denoting time-average. Recall that the tangent vector $\boldsymbol{\delta}$ satisfies the variational equation:

$$\dot{\boldsymbol{\delta}} = \Lambda(\gamma(t))\boldsymbol{\delta}, \tag{5}$$

where $\Lambda = D\boldsymbol{v}$ is the Jacobian matrix of the vector field $\boldsymbol{v}$.

We now introduce the MEGNO, $Y(\gamma(t))$, through the expression

$$Y(\gamma(t)) = \frac{2}{t} \int_0^t \frac{\dot{\delta}(\gamma(t'))}{\delta(\gamma(t'))} t'\, \mathrm{d}t', \tag{6}$$

which is somewhat related to the integral appearing in (4). Notice that in the case of an exponential increase of δ, $\delta(\gamma(t)) = \delta_0 \exp(\lambda t)$, the quantity $Y(\gamma(t))$ can be considered as a weighted variant of the integral in (4). Indeed, instead of the instantaneous rate of increase, λ, we average the logarithm of the growth factor, $\ln(\delta(\gamma(t))/\delta_0) = \lambda t$. Further variants are to be considered in Section 4.

Let us now look for MEGNO's asymptotic behavior for some, though quite special, very representative solutions of (5) in order to show how $Y(\gamma(t))$ serves to give clear indication on the character of the different orbits.

In the first place we consider orbits on irrational tori for a non-isochronous system. For any such a (quasi-periodic) orbit, γ_q, the solution of (5) in $\mathbb{R}^{2N}$ has the form:

$$\delta(\gamma_q(t)) \approx \delta_0[1 + w_q(t) + t(\lambda_q + u_q(t))], \tag{7}$$

where $\lambda_q > 0$ is the linear rate of divergence around γ_q, and $w_q(t)$ and $u_q(t)$ are the oscillating functions of t (in general quasi-periodic and with zero average) of bounded amplitude, satisfying $|u_q(t)| \leq b_q < \lambda_q$. The parameter λ_q is a measure of the lack of isochronicity around the orbit since it is related to the maximum eigenvalue of the matrix $\partial\boldsymbol{\omega}/\partial\boldsymbol{I}$, $\boldsymbol{\omega}$ and $\boldsymbol{I}$ being the frequency and action vectors associated to the torus, respectively (for an isochronous system, such as the harmonic oscillator, $\lambda = 0$ for all γ). Then, from (6) and (7), and recalling that u_q is bounded by b_q, it is straightforward to show that $Y(\gamma_q(t))$ oscillates with bounded amplitude about the value 2 verifying

$$|Y(\gamma_q(t)) - 2| \leq 4 \ln \frac{\lambda_q + b_q}{\lambda_q - b_q} \approx 8\frac{b_q}{\lambda_q}, \quad t \to \infty, \tag{8}$$

where the last approximation holds provided that $b_q \ll \lambda_q$. The temporal evolution of $Y(\gamma_q(t))$ is given by

$$Y(\gamma_q(t)) \approx 2 - \frac{\ln(1 + \lambda_q t)^2}{\lambda_q t} + O(\gamma_q(t)), \tag{9}$$

where O denotes an oscillating term (with zero average) due to the quasi-periodic character of both $w_q(t)$ and $u_q(t)$. The $\lim_{t\to\infty} Y(\gamma_q(t))$ does not exist but, on introducing the time-average:

$$\bar{Y}(\gamma_q(t)) \equiv \frac{1}{t}\int_0^t Y(\gamma_q(t'))\,\mathrm{d}t', \tag{10}$$

it can readily be shown from (8)–(10) that

$$\bar{Y}(\gamma_q) \equiv \lim_{t\to\infty} \bar{Y}(\gamma_q(t)) = 2. \tag{11}$$

Therefore, for the case of quasi-periodic motion, $\bar{Y}(\gamma)$ is a fixed constant, independent of γ.

The above given results still hold in the case of a regular orbit γ that is not purely stable quasi-periodic. (We will restrict ourselves to 2D Hamiltonian systems, though the arguments given below could be straightforwardly extended to higher dimensions.) Let γ be close to a stable periodic orbit, γ_s. Since $O(\gamma(t))$ in (9) involves nearly periodic terms, and both λ and b/λ are small, it follows from (8) and (9) that $Y(\gamma(t))$ oscillates with small amplitude about 2 and that $\bar{Y}(\gamma_q)$ converges to 2 slower the smaller is λ. When $\gamma \to \gamma_s$, both $u(t), \lambda \to 0$, and $\bar{Y} \to 0$ as $t \to \infty$. In this limiting case, the oscillations of $Y(\gamma(t))$ about the value 0 are due to the presence of the term $w(t)$ in (7).

A rather different behaviour of $Y(\gamma(t))$ should be expected whenever γ is close to an unstable periodic orbit, γ_u. In such a case, the motion in any small neighborhood of γ_u, V, is mainly determined by its associated stable and unstable manifolds. For sufficiently large motion times, γ will pass close to γ_u several times. Suppose that between two successive close approaches with γ_u, γ spends a time Δt_1 within V and a time Δt_2 outside it. During the interval Δt_1, it is $\delta(\gamma(t)) \approx \delta(\gamma_u(t)) \approx \delta_0 \exp(\mu t)$ with $\mu > 0$, while, during Δt_2, $\delta(\gamma(t))$ approximately obeys (7). The "interaction time" between γ and γ_u, Δt_1, is larger the closer the orbits are to each other. Thus, $Y(\gamma(t))$

should exhibit quasi-periodic oscillations modulated by periodic pulses, of period $\sim\Delta t_2$, width $\sim\Delta t_1$ and similar amplitude. Analogous considerations apply to $\bar{Y}(\gamma(t))$ but, due to the averaging, the amplitude of the pulses should decrease as $\sim 1/t$. In general, $\bar{Y}(\gamma(t))$ will approach the value 2 from above and, after a total motion time t, $\bar{Y}(\gamma(t))$ will be larger the smaller is the distance $|\gamma-\gamma_{\rm u}|$. In the limit, when $\gamma\to\gamma_{\rm u}$, $\Delta t_1\approx t$ and $\bar{Y}(\gamma(t))$ grows unboundedly, so that $\bar{Y}(\gamma(t))\gg 2$ (see Eq. (13)).

In the case of an irregular orbit, $\gamma_{\rm i}$, within any stochastic component, we have $\delta(\gamma_{\rm i}(t))\approx\delta_0\exp(\sigma_i t)$, σ_i being $\gamma_{\rm i}$'s LCN. Thus, it is

$$Y(\gamma_{\rm i}(t))\approx\sigma_i t+\tilde{O}(\gamma_{\rm i}(t)) \tag{12}$$

with $\tilde{O}$ some oscillating term of bounded amplitude (which is in general neither periodic nor quasi-periodic, but it has zero average). On averaging over an interval large enough, we get

$$\bar{Y}(\gamma_{\rm i}(t))\approx\tfrac{1}{2}\sigma_i t,\quad t\to\infty. \tag{13}$$

Therefore, for a chaotic orbit, $Y(\gamma_{\rm i}(t))$ and $\bar{Y}(\gamma_{\rm i}(t))$ grow linearly with time, at a rate equal to the LCN of the orbit or one-half of it, respectively (see below, however). Only when the phase space has an hyperbolic structure, does Y grow with time. Otherwise, it saturates to a constant value, even in the degenerated cases in which δ grows with some power of t, say n, where $\bar{Y}\to 2n$ as $t\to\infty$.

Let us note that MEGNO's temporal evolution allows for being summed up in a single expression valid for any kind of motion, which is certainly not the case for σ_1. Indeed, the asymptotic behaviour of $\bar{Y}(\gamma(t))$ may be written in the fashion $\bar{Y}(\gamma(t))\approx a_\gamma t+d_\gamma$, where $a_\gamma=\sigma_\gamma/2$ and $d_\gamma\approx 0$ for irregular, stochastic motion, while $a_\gamma=0$ and $d_\gamma\approx 2$ for stable quasi-periodic motion. Departures from the value $d_\gamma\approx 2$ indicate that γ is close to some periodic orbit, being $d_\gamma\lesssim 2$ and $d_\gamma\gtrsim 2$ for stable and unstable periodic orbits, respectively.

Finally, notice that the quantity $\hat{\sigma}_1=Y/t$ verifies

$$\hat{\sigma}_1(\gamma_q(t))\approx\frac{2}{t},\qquad \hat{\sigma}_1(\gamma_{\rm i}(t))\approx\sigma_i,\quad t\to\infty, \tag{14}$$

which show that, in the case of regular motion, $\hat{\sigma}_1$ converges to 0 faster than σ_1 does (which goes to zero as $\ln t/t$), while for chaotic motion both magnitudes approach the positive LCN at a rather similar rate.

As it turns out from Eqs. (11) and (13), the LCN can be recovered by means of a simple linear least squares fit on $\bar{Y}(\gamma_{\rm i}(t))$. The main feature of this procedure is that it takes advantage of the dynamical information contained in $\bar{Y}(\gamma_{\rm i}(t))$ regarding the whole interval $(0,t)$ and of the fact that $\bar{Y}$ has a smooth character. Since for purely quasi-periodic orbits $\bar{Y}(\gamma(t))$ approach the constant value 2 quite faster than for nearly stable and unstable periodic orbits, the LCN derived from the MEGNO will also provide us with information on elliptic and hyperbolic points as well.

In order to illustrate the announced MEGNO's behaviour, we consider the well-known 2D Hénon–Heiles model [18] for the energy level $h=0.118$, the characteristic period of motion being $T\sim 10$. The phase space at this energy level displays at least two main unconnected chaotic domains having different LCNs (see, for instance, [8]). One of these domains is associated to simple hyperbolic periodic orbits, while the other is related to 5-periodic orbits around a simple elliptic periodic orbit.

We picked up the initial conditions of five representative orbits from the surface $x=0$: one close to a stable 1-periodic orbit at $(y,\,p_y)=(0.295456,\,0)$ (sp); another one looking like stable quasi-periodic at (0.483, 0) (qp); a third one at (0.46912, 0) also quasi-periodic but close to an unstable 4-periodic orbit (up); two irregular orbits, one inside a gross stochastic layer (c1) at (0.509, 0), and the other one lying in a large chaotic sea (c2) at (0.56, 0.112).

We computed Y and $\bar{Y}$ by means of (6) and (10), respectively; note that the renormalization of $\boldsymbol{\delta}$, if necessary, proceeds naturally from (6). The numerical integrations were performed by means of a Runge–Kutta 7/8th order integrator (the so-called Dopri8 routine, see [17,24], the accuracy in the conservation of the energy being $\sim 10^{-13}$.

In Fig. 1 we show that both Y and $\bar{Y}$ evolve with time as predicted by Eqs. (9), (11)–(13). Indeed, in Fig. 1a we observe that, for the stable quasi-periodic orbit (qp), $Y(t)$ oscillates about the value 2 with an amplitude $\lesssim 1$, while $\bar{Y}(t)$ shows a very fast convergence to the actual average (see below).

Fig. 1b displays the typical behaviour of a trajectory close to an unstable periodic orbit. While the (up) orbit is "far away" from the hyperbolic point, both $Y(t)$ and $\bar{Y}(t)$ evolve as in the previous case. However, when the quasi-periodic orbit passes close to the unstable one, the mutual interaction causes the oscillations of $Y(t)$ to exhibit a strong modulation, which is damped in $\bar{Y}(t)$ as t increases. Thus, after the first close approach at $t \sim 2000$, $\bar{Y}(t) > 2$ (due mainly to the cumulative effect on the average) but, for t large enough, it asymptotically approaches the value 2.

Also for the irregular orbits (c1) and (c2) did we compute the time evolution of Y and $\bar{Y}$. The results are given in Fig. 1c, where both $Y(t)$ and $2\bar{Y}(t)$ are plotted together to show that, as follows from Eqs. (12) and (13), both quantities have the same time-rate. Since the trajectories belong to unconnected chaotic domains, the time-rate (i.e. the LCN) is different for the two orbits.

In Fig. 1d, the temporal evolution of $\bar{Y}$ for all the three regular orbits are compared. For the stable quasi-periodic orbit (qp), $\bar{Y}$ reaches the value 2 much faster than for the orbit (sp), which is close to a stable periodic one. In fact, $\bar{Y}(\gamma_{\rm sp}) \lesssim 2$ over all the time interval. Both curves, the one for $\bar{Y}(\gamma_{\rm sp})$ and that for $\bar{Y}(\gamma_{\rm qp})$, fit very well Eq. (9), on neglecting oscillations, being $\lambda_{\rm sp} < \lambda_{\rm qp}$. Again, we note that the orbits (qp) and (up) evolve in a rather similar way, as long as the interaction between (up) and its nearby unstable periodic orbit is weak.

In order to show that actually $\hat{\sigma}_1 \to$ LCN when $t \to \infty$, in Fig. 1e we display its time evolution together with that of σ_1 for three of the orbits, namely, (sp), (c1) and (c2). We observe that for the chaotic orbits, both magnitudes converge to the same positive LCN at the same rate. Only there are very small differences between $\hat{\sigma}_1$ and σ_1 (see below). For the regular orbit (sp) instead, we note that $\hat{\sigma}_1$ decreases faster than σ_1, the expected final values (see Eq. (14) and discussion below), 0.00013 and 0.00064, respectively, being in good agreement with the computed ones.

In the case of chaotic motion, both Y and $\bar{Y}$ evolve almost linearly with time along the whole time interval, as seen in Fig. 1c. The deviations from the linear trend, for instance, in (c2), are presumably caused by stickiness. Indeed, during those time intervals in which Y is almost flat, the orbit remains close to some small stability domain embedded in the chaotic sea. Here, stickiness does not significantly reduce fast diffusion but, whenever it is strong, it does influence the mean time-rate of both Y and $\bar{Y}$ and consequently, the derived LCN. In order to illustrate this effect, let us consider the differential equation $\dot{x} = a(t)x$, $x \in \mathbb{R}$, with $a(t)$ a real valued function, so that the LCN is

$$\sigma = \lim_{t\to\infty} \frac{1}{t} \int_0^t a(t')\,{\rm d}t'. \tag{15}$$

If we compute both the LCN and Y for a finite time interval T and the function $a(t)$ taking the value a_1 for $0 \le t \le T/2$, and a_2 for $T/2 \le t \le T$, with a_1 and a_2 constants, then there results $\sigma = \sigma_1 = (a_1 + a_2)/2$. Meanwhile, the MEGNO, given by (6), is

$$Y = \frac{2}{T} \int_0^T a(t')t'\,{\rm d}t' = \frac{a_1 + 3a_2}{4} T. \tag{16}$$

We see that, in this case, the relative error, $\varepsilon = |\hat{\sigma}_1 - \sigma_1|/\sigma_1 = |a_2 - a_1|/|2(a_1 + a_2)|$, is maximum when any of the $a_i \to 0$, yielding $\varepsilon = 1/2$, while it takes its minimum value, $\varepsilon = 0$, for $a_1 = a_2$. This rather simple example serves to illustrate that, even in the case of fairly strong stickiness, the rate at which Y evolves does not differ much from that of the LCN. Here, for instance, the difference barely amounts a factor 1.5.

Further details on the MEGNO's performance when applied to the study of global dynamics in 2D Hamiltonians, as well as the advantages of deriving the LCN from a least squares fit on $\bar{Y}$ are given in [6,7]. An interesting

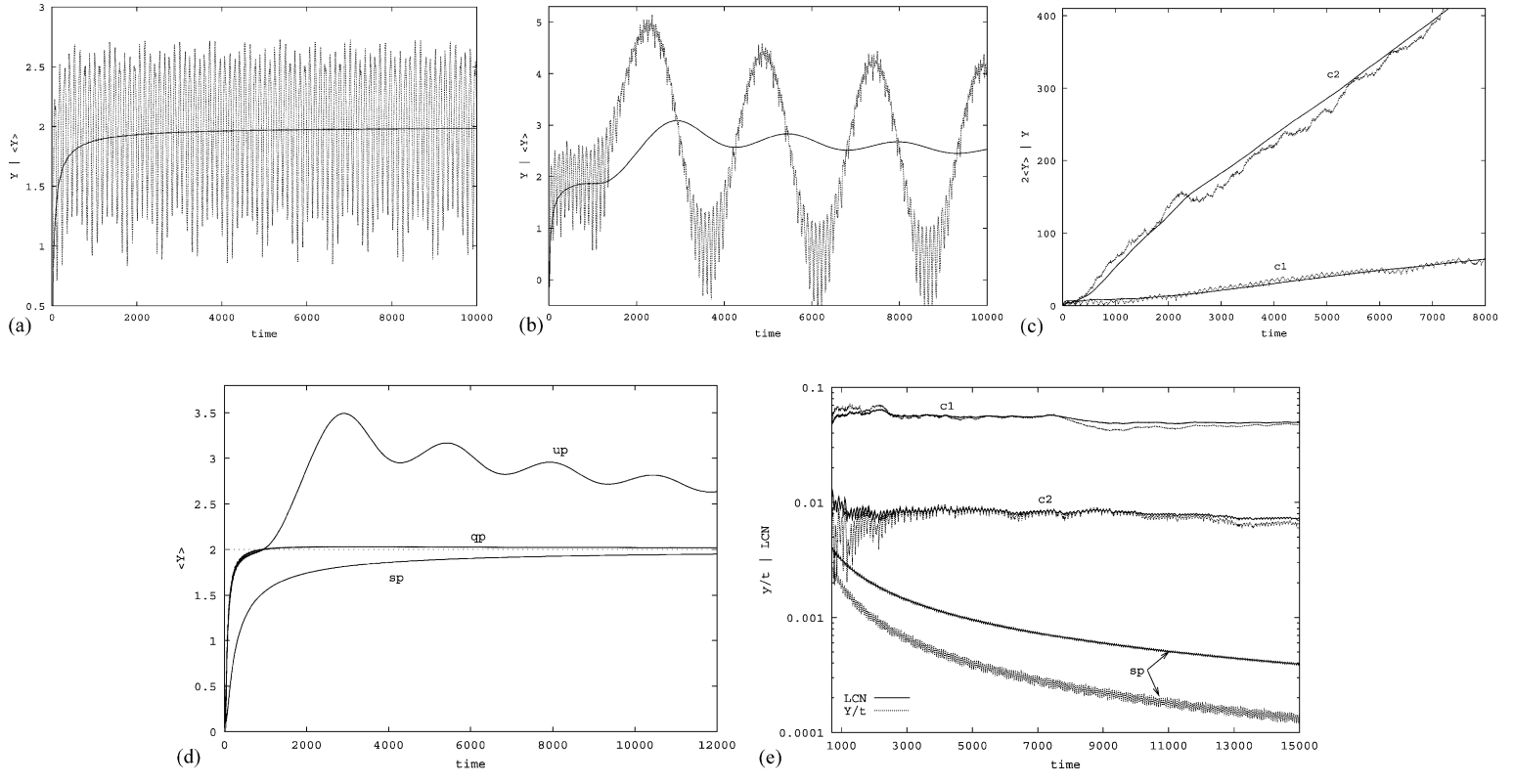

Fig. 1. Time evolution of Y and $\bar{Y}$ ($\langle Y\rangle$ in the figure) for typical orbits: (a) (qp) stable quasi-periodic; (b) (up) quasi-periodic but close to an unstable 4-periodic orbit; (c) (c1) and (c2) irregular, embedded in two different stochastic domains (smooth curves corresponding to $2\bar{Y}$, and noisy curves to Y). (d) $\bar{Y}$ ($\langle Y\rangle$ in the figure) for three regular orbits: (sp) close to a stable periodic, (qp), and (up); (e) time evolution of $\hat{\sigma}_1$ (Y/t in the figure) and the finite time Lyapunov exponent σ_1 (denoted by LCN in the figure) for (sp), (c1) and (c2).

application to a 2.5D problem, namely, the Arnold's classical problem of diffusion when the two small parameters are equal, may be found in [25]. The associated splitting of separatrices has been studied in [27].

3. A 3D model

Below, we consider a toy 3D model in order to illustrate how the MEGNO technique succeeds in providing a detailed picture of its resonance structure. With this aim we address the perturbed quartic oscillator. Indeed, for this rather simple model the different resonances for small values of the perturbation parameter are easily identified so that the comparison with the MEGNO's results is straightforward.

Therefore we investigate the full dynamics of the system:

$$\tilde{H}(\boldsymbol{p},\boldsymbol{q}) = \tfrac{1}{2}\boldsymbol{p}^2 + \tfrac{1}{4}(x^4+y^4+z^4) + \epsilon x^2(y+z) \tag{17}$$

on a given energy surface and for different values of the parameter ϵ. The term $\epsilon\tilde{V}(x,y,z) = \epsilon x^2(y+z)$ can be regarded as a small perturbation to the integrable 3D uncoupled quartic oscillator, as long as $\epsilon \ll 1$. Recall that the quartic oscillator allows for the analytic solution $q(t) = a\,\mathrm{cn}(at)$, where a is the oscillation amplitude and $\mathrm{cn}(u)$ is the Jacobian elliptic cosine (see [5]). Using the Fourier expansion for $\mathrm{cn}(u)$ (see [16]) and writing the amplitude in terms of the energy, h, $q(t)$ can be recast as

$$q(t) = q_0(h)\sum_{n=1}^{\infty}\alpha_n\cos((2n-1)\omega t)), \quad q_0 = 4\beta h^{1/4}, \ \ \omega = \sqrt{2}\beta h^{1/4}, \ \ \beta = \frac{\pi}{2K(1/\sqrt{2})}, \tag{18}$$

where $K(k)$ denotes the complete elliptic integral, and the coefficients in the Fourier expansion are given by

$$\alpha_n = \frac{1}{\cosh((n-1/2)\pi)}, \qquad \frac{\alpha_{n+1}}{\alpha_n} \approx \mathrm{e}^{-\pi} \approx \frac{1}{23}. \tag{19}$$

In terms of the unperturbed action-angle variables, $(I_1, I_2, I_3; \theta_1, \theta_2, \theta_3)$, Hamiltonian (17) can be written as

$$H(\boldsymbol{I},\boldsymbol{\theta}) = H_0(\boldsymbol{I}) + \epsilon V(\boldsymbol{I},\boldsymbol{\theta}), \tag{20}$$

where H_0 is given by

$$H_0(\boldsymbol{I}) = A(I_1^{4/3} + I_2^{4/3} + I_3^{4/3}) \tag{21}$$

with $A = (3\beta/2\sqrt{2})^{4/3}$, and the perturbation admits of the Fourier expansion:

$$\begin{aligned} V(\boldsymbol{I},\boldsymbol{\theta}) = {} & \hat{V}_{12}\sum_{n,m,k=1}^{\infty}\alpha_{nmk}(\cos(2(n+m-1)\theta_1 \pm (2k-1)\theta_2) + \cos(2(n-m)\theta_1 \pm (2k-1)\theta_2)) \\ & + \hat{V}_{13}\sum_{n,m,k=1}^{\infty}\alpha_{nmk}(\cos(2(n+m-1)\theta_1 \pm (2k-1)\theta_3) + \cos(2(n-m)\theta_1 \pm (2k-1)\theta_3)), \end{aligned} \tag{22}$$

the function $\hat{V}_{ij}$ and the coefficients α_{nmk} being

$$\hat{V}_{ij} \equiv \hat{V}(I_i, I_j) = C I_i^{2/3} I_j^{1/3}, \quad C = \frac{3\beta}{4}, \qquad \alpha_{nmk} = \alpha_n\alpha_m\alpha_k.$$

The unperturbed frequency vector is

$$\boldsymbol{\omega}(\boldsymbol{I}) = \frac{\partial H_0}{\partial \boldsymbol{I}} = \frac{4}{3}A(I_1^{1/3}, I_2^{1/3}, I_3^{1/3}). \tag{23}$$

In order to easily visualize the resonance structure on the energy surface, we introduce a first change of coordinates, such that the unperturbed energies in each degree of freedom, h_1, h_2, h_3, become the new action-like variables. Then we get

$$H_0(h_1, h_2, h_3) = h_1 + h_2 + h_3, \qquad \boldsymbol{\omega}(h_1, h_2, h_3) = \sqrt{2}\beta(h_1^{1/4}, h_2^{1/4}, h_3^{1/4})$$

and, in terms of h_1 and h_2, the resonance condition, $\boldsymbol{m} \cdot \boldsymbol{\omega} = 0$, $\boldsymbol{m} \in \mathbb{Z}^3/\{\mathbf{0}\}$, for $H_0 = h$ reads

$$(m_1^4 + m_3^4)\xi^4 + 4m_1^3 m_2 \xi^3 \eta + 6m_1^2 m_2^2 \xi^2 \eta^2 + 4m_1 m_2^3 \xi \eta^3 + (m_2^4 + m_3^4)\eta^4 - m_3^4 = 0, \tag{24}$$

where $\xi = (h_1/h)^{1/4}$, $\eta = (h_2/h)^{1/4}$.

Let us now look for the strength of the different harmonics in perturbation (22). On keeping terms of $\mathcal{O}(1)$ in the coefficients, i.e. neglecting all terms with $n, m, k > 1$, the harmonics of largest amplitude are

$$\mathcal{A}_\epsilon^0 = \{(2, \pm 1, 0), (2, 0, \pm 1), (0, \pm 1, 0), (0, 0, \pm 1)\},$$

while, retaining terms up to $\mathcal{O}(1/23)$, we obtain

$$\mathcal{A}_\epsilon^1 = \mathcal{A}_\epsilon^0 \cup \{(4, \pm 1, 0), (4, 0, \pm 1), (2, \pm 3, 0), (2, 0, \pm 3), (-2, \pm 1, 0), (-2, 0, \pm 1), (0, \pm 3, 0), (0, 0, \pm 3)\}$$

and, at $\mathcal{O}(1/23^2)$

$$\mathcal{A}_\epsilon^2 = \mathcal{A}_\epsilon^1 \cup \{(6, \pm 1, 0), (6, 0, \pm 1), (4, \pm 3, 0), (4, 0, \pm 3), (2, \pm 5, 0), (2, 0, \pm 5), (-2, \pm 3, 0), (-2, 0, \pm 3), (-4, \pm 1, 0), (-4, 0, \pm 1), (0, \pm 5, 0), (0, 0, \pm 5)\}.$$

We will now be concerned with harmonics appearing at order $\mathcal{O}(\epsilon^2)$ and then introduce a canonical transformation F: $(\boldsymbol{I}, \boldsymbol{\theta}) \mapsto (\boldsymbol{J}, \boldsymbol{\varphi})$:

$$F(\boldsymbol{J}, \boldsymbol{\theta}) = \boldsymbol{J} \cdot \boldsymbol{\theta} + \epsilon \Phi(\boldsymbol{J}, \boldsymbol{\theta}), \qquad \boldsymbol{I} = \frac{\partial F}{\partial \boldsymbol{\theta}}, \qquad \boldsymbol{\varphi} = \frac{\partial F}{\partial \boldsymbol{J}}, \qquad \mathcal{H}(\boldsymbol{J}, \boldsymbol{\varphi}) = H(\boldsymbol{I}, \boldsymbol{\theta}) \tag{25}$$

with the function $\Phi(\boldsymbol{J}, \boldsymbol{\theta})$ so chosen that the transformed Hamiltonian $\mathcal{H}$ does not contain terms of $\mathcal{O}(\epsilon)$, which of course can be done as long as we are "far away" from any primary resonance (see below). Thus, introducing $\boldsymbol{I} = \boldsymbol{J} + \epsilon \nabla_\theta \Phi$ in $H_0(\boldsymbol{I})$, and expanding it up to the second order in ϵ, we obtain

$$H_0(\boldsymbol{I}) = H_0(\boldsymbol{J}) + \epsilon \boldsymbol{\omega} \cdot \nabla_\theta \Phi + \frac{1}{2}\epsilon^2 \frac{\partial \omega_i}{\partial I_j} \Phi_{\theta_i} \Phi_{\theta_j} + \mathcal{O}(\epsilon^3), \tag{26}$$

$\boldsymbol{\omega}$ being the unperturbed frequency vector given by (23); here, $\partial \omega_i / \partial I_j$ stands for $(\partial \omega_i / \partial J_j)_{\boldsymbol{J}=\boldsymbol{I}}$, and the sum over repeated indexes should be understood. But, since the Jacobian matrix, $\partial \omega_i / \partial I_j$, is diagonal, (26) reduces to

$$H_0(\boldsymbol{I}) \approx H_0(\boldsymbol{J}) + \epsilon \boldsymbol{\omega} \cdot \nabla_\theta \Phi + \frac{1}{2}\epsilon^2 \frac{\partial \omega_i}{\partial I_i} (\Phi_{\theta_i})^2. \tag{27}$$

Let us now split perturbation (22) into two, namely V_{xy} and V_{xz}, which, by introducing the integer vectors $\boldsymbol{l} = (l_1, l_2, 0)$, $\boldsymbol{k} = (k_1, 0, k_3)$ and the new coefficients $\hat{\alpha}_{l_1 l_2}$ and $\hat{\alpha}_{k_1 k_3}$, read

$$V_{xy}(I_1, I_2; \theta_1, \theta_2) = \hat{V}_{12} \sum_{l_1, l_2} \hat{\alpha}_{l_1 l_2} \cos(l_1 \theta_1 + l_2 \theta_2), \qquad V_{xz}(I_1, I_3; \theta_1, \theta_3) = \hat{V}_{13} \sum_{k_1, k_3} \hat{\alpha}_{k_1 k_3} \cos(k_1 \theta_1 + k_3 \theta_3)$$

so that the full Hamiltonian, up to $\mathcal{O}(\epsilon^2)$, becomes

$$\mathcal{H}(\boldsymbol{J}, \boldsymbol{\theta}) \approx H_0(\boldsymbol{J}) + \epsilon(\boldsymbol{\omega} \cdot \nabla_\theta \Phi + V_{xy} + V_{xz}) + \frac{1}{2}\epsilon^2 \frac{\partial \omega_i}{\partial I_i} (\Phi_{\theta_i})^2. \tag{28}$$

Therefore, in order to avoid terms of $\mathcal{O}(\epsilon)$ in $\mathcal{H}$, the function Φ should be of the form:

$$\Phi(\boldsymbol{J},\boldsymbol{\theta}) = \sum_{l_1,l_2} \phi^{(1)}_{l_1 l_2} \sin(l_1\theta_1 + l_2\theta_2) + \sum_{k_1,k_3} \phi^{(2)}_{k_1 k_3} \sin(k_1\theta_1 + k_3\theta_3) \tag{29}$$

with the amplitudes verifying

$$\phi^{(1)}_{l_1 l_2} = -\frac{\hat{V}_{12}\hat{\alpha}_{l_1 l_2}}{l_1\omega_1 + l_2\omega_2}, \qquad \phi^{(2)}_{k_1 k_3} = -\frac{\hat{V}_{13}\hat{\alpha}_{k_1 k_3}}{k_1\omega_1 + k_3\omega_3}. \tag{30}$$

Hence, provided that $l_1\omega_1 + l_2\omega_2 \neq 0$ and $k_1\omega_1 + k_3\omega_3 \neq 0$, all terms of order ϵ will be removed from the Hamiltonian. Actually, the non-resonance condition should be stated properly in terms of a suitable Diophantine condition in order to avoid too small divisors in (29). Thus, being "far away" from primary resonances, (28) reduces to

$$\mathcal{H}(\boldsymbol{J},\boldsymbol{\theta}) \approx H_0(\boldsymbol{J}) + \frac{1}{2}\epsilon^2 \frac{\partial\omega_i}{\partial I_i}(\Phi_{\theta_i})^2. \tag{31}$$

Let us note that the presence of $(\Phi_{\theta_i})^2$ leads to new harmonics. Indeed, on computing $(\Phi_{\theta_1})^2$ we obtain

$$\sum_{\boldsymbol{l},\boldsymbol{l}'} \phi^{(1)}_{\boldsymbol{l}}\phi^{(1)}_{\boldsymbol{l}'} l_1 l'_1 \cos(\boldsymbol{l}\cdot\boldsymbol{\theta})\cos(\boldsymbol{l}'\cdot\boldsymbol{\theta}) + \sum_{\boldsymbol{k},\boldsymbol{k}'} \phi^{(2)}_{\boldsymbol{k}}\phi^{(2)}_{\boldsymbol{k}'} k_1 k'_1 \cos(\boldsymbol{k}\cdot\boldsymbol{\theta})\cos(\boldsymbol{k}'\cdot\boldsymbol{\theta})$$
$$+ 2\sum_{\boldsymbol{k},\boldsymbol{l}} \phi^{(1)}_{\boldsymbol{l}}\phi^{(2)}_{\boldsymbol{k}} l_1 k_1 \cos(\boldsymbol{l}\cdot\boldsymbol{\theta})\cos(\boldsymbol{k}\cdot\boldsymbol{\theta}),$$

all degrees of freedom being coupled in the last term. When computing $(\Phi_{\theta_2})^2$ and $(\Phi_{\theta_3})^2$, instead, degrees of freedom 2 and 3 remain uncoupled. The new harmonics corresponding to $\boldsymbol{l},\boldsymbol{k} \in \mathcal{A}^0_\epsilon$ which verify that $|\boldsymbol{m}| < 5$ are

$$\mathcal{A}^0_{\epsilon^2} = \{(4,0,0),(\pm2,0,0),(0,\pm2,0),(0,0,\pm2),(0,\pm1,\pm1),(\pm2,\pm2,0),(\pm2,0,\pm2)\},$$

while, retaining terms up to $\mathcal{O}(1/23^2)$ also satisfying that $|\boldsymbol{m}| < 5$, we obtain

$$\mathcal{A}^2_{\epsilon^2} = \mathcal{A}^1_{\epsilon^2} = \mathcal{A}^0_{\epsilon^2} \cup \{(-4,0,0),(0,\pm4,0),(0,0,\pm4),(0,\pm1,\pm3),(0,\pm3,\pm1),(\pm2,\pm1,\pm1)\}.$$

From $\mathcal{A}^0_\epsilon$, $\mathcal{A}^1_\epsilon$, $\mathcal{A}^2_\epsilon$, $\mathcal{A}^0_{\epsilon^2}$, $\mathcal{A}^1_{\epsilon^2}$ and $\mathcal{A}^2_{\epsilon^2}$ we learn which harmonics would become a resonance (since the ω_i's are always positive) and at which order, in both the coefficients of the expansion and the perturbation parameter, they would appear.

Note that for those harmonics in which one of the m_i is zero, the resonant polynomial (24) can be easily solved to yield

$$\hat{h}_2 = \frac{m_1^4}{m_2^4}\hat{h}_1, \qquad m_1 m_2 < 0, \qquad m_3 = 0, \tag{32a}$$

$$\hat{h}_2 = 1 - \left(\frac{m_1^4 + m_3^4}{m_3^4}\right)\hat{h}_1, \qquad m_1 m_3 < 0, \qquad m_2 = 0, \tag{32b}$$

$$\hat{h}_2 = \left(\frac{m_3^4}{m_2^4 + m_3^4}\right)(1 - \hat{h}_1), \qquad m_2 m_3 < 0, \qquad m_1 = 0 \tag{32c}$$

with $\hat{h}_i = h_i/h$, showing that those resonances associated to resonant vectors with at least one null m_i, appear as straight lines on the energy surface $\hat{h}_1 + \hat{h}_2 + \hat{h}_3 = 1$.

The width of any of those resonances can be computed by means of a simple pendulum approximation, which indeed is a suitable description whenever we assume each resonance to be isolated from the rest. Let us, for example, take a resonance at $\mathcal{O}(\epsilon)$, the resonant vector being $\boldsymbol{m} = (m_1, -m_2, 0)$, with $m_1, m_2 > 0$. Its amplitude, assuming order $\mathcal{O}(1)$ for the coefficients, is

$$V_{\boldsymbol{m}} = \hat{V}_{12}\alpha_1^3 = \tfrac{3}{4}\beta\alpha_1^3 I_1^{\mathrm{r}2/3} I_2^{\mathrm{r}1/3}, \tag{33}$$

but, since the resonant values I_1^{r} and I_2^{r} verify $m_1\omega_1(I_1^{\mathrm{r}}) - m_2\omega_2(I_2^{\mathrm{r}}) = 0$, which yields $I_2^{\mathrm{r}} = (m_1/m_2)^3 I_1^{\mathrm{r}}$, there results

$$V_{\boldsymbol{m}} = \frac{3\beta}{4}\frac{m_1}{m_2}\alpha_1^3 I_1^{\mathrm{r}}. \tag{34}$$

Then, the amplitude depends only on I_1^{r}, which varies on the interval $(0, I_*(h))$, with I_* defined through both the resonance condition and the energy conservation. Notice that resonances of the form $\omega_1 = 0$, $\omega_2 = 0$ or $\omega_3 = 0$ should not show up since their corresponding amplitudes are zero.

In action space the width of the resonance is given by the vector (see [5]):

$$(\boldsymbol{\Delta I})^{\mathrm{r}}_{\boldsymbol{m}} = \boldsymbol{m}\sqrt{\epsilon M V_{\boldsymbol{m}}}, \qquad \frac{1}{M} = m_i\left(\frac{\partial\omega_i}{\partial I_j}\right)_{\boldsymbol{I}^{\mathrm{r}}} m_j = m_1^2\left(\frac{\partial\omega_1}{\partial I_1}\right)_{\boldsymbol{I}^{\mathrm{r}}} + m_2^2\left(\frac{\partial\omega_2}{\partial I_2}\right)_{\boldsymbol{I}^{\mathrm{r}}} \tag{35}$$

and, in the h_i action-like variables, it can be computed as (see below)

$$(\Delta h_i)^{\mathrm{r}}_{\boldsymbol{m}} = \omega_i^{\mathrm{r}}(\Delta I_i)^{\mathrm{r}}_{\boldsymbol{m}}, \tag{36}$$

where $(\Delta h_i)^{\mathrm{r}}_{\boldsymbol{m}}$ and $(\Delta I_i)^{\mathrm{r}}_{\boldsymbol{m}}$ denote the ith-component of vectors $(\boldsymbol{\Delta h})^{\mathrm{r}}_{\boldsymbol{m}}$ and (35), respectively. A straightforward calculation leads to

$$(\Delta h_i)^{\mathrm{r}}_{\boldsymbol{m}} = (-1)^{(i-1)}2^{3/4}K_{\boldsymbol{m}}\sqrt{\alpha_1^3\epsilon h_1^{r7/8}}, \quad K_{\boldsymbol{m}} = \sqrt{\frac{m_1/m_2}{1+(m_2/m_1)^4}}, \quad i = 1, 2. \tag{37}$$

Then, since $(\Delta h_1)^{\mathrm{r}}_{\boldsymbol{m}} = -(\Delta h_2)^{\mathrm{r}}_{\boldsymbol{m}}$ and $m_3 = 0$, the width (half-width to be precise) in energy space is $\sqrt{2}$ times the amount given by (37). Numerical factors aside, the width, being $\sim\alpha_1^{3/2}\sqrt{\epsilon}h_1^{r7/8}$, increases almost linearly with h_1^{r}. For resonances at $\mathcal{O}(1/23)$ or $\mathcal{O}(1/23^2)$, the width is about $1/\sqrt{23} \approx 1/5$ or $1/23$, respectively, of that given by (37). Just to give an idea of the order of magnitude of the theoretical resonance widths, let us say that the maximum width of one of the strongest resonances, i.e. $(2, -1, 0)$, is about $\sqrt{\epsilon}/10$.

Eq. (37) also provides the width of resonances of the type $(m_1, 0, -m_3)$, when replacing therein m_2 by m_3, whether the minus sign is taken up on computing $(\Delta h_3)^{\mathrm{r}}_{\boldsymbol{m}}$. For $(0, m_2, -m_3)$ resonances, however, (37) does no longer apply since they appear but at $\mathcal{O}(\epsilon^2)$, as follows from $\mathcal{A}^0_{\epsilon^2}$. In such a case, we know that the width is $\sim\epsilon$, but we would need to calculate their amplitudes in order to obtain the dependence on both h_1^{r} and the harmonic numbers.

Let us observe that the relation $(\Delta h_1)^{\mathrm{r}}_{\boldsymbol{m}} = -(\Delta h_2)^{\mathrm{r}}_{\boldsymbol{m}}$ is a natural consequence of the change of coordinates performed. Indeed, the map $\boldsymbol{I} \mapsto \boldsymbol{h}$ transforms the unperturbed energy surface, M_h, into a plane, so that the normal vector (covector) to M_h becomes constant, $\boldsymbol{\omega} \mapsto (1, 1, 1)$ and $m^i \mapsto m^l\omega_l\delta^i_l$. Then, the invariant resonance condition, $\boldsymbol{m}\cdot\boldsymbol{\omega} = 0$, yields, in the new coordinates, the resonant vector $(s, -s, 0)$, with $s = m^1\omega_1^{\mathrm{r}} = m^2\omega_2^{\mathrm{r}}$. Clearly, analogous results are obtained for any resonance with one null m^i. Whenever all the $m^i \neq 0$, the resonant vector becomes $(s^1, s^2, -s^1 - s^2)$, with $s^i = m^l\omega_l^{\mathrm{r}}\delta^i_l$. From the above discussion it follows that (36) is just the law under which the components of any vector should transform under the given change of coordinates.

Now, in order to have the actual motion on M_h, let us perform a second (global) change of coordinates in such a way that one of the new basis vectors, say $\boldsymbol{n}_3$ is normal to M_h, namely, $\boldsymbol{n}_3 = (1, 1, 1)/\sqrt{3}$. The remainder basis

vectors are taken on M_h and orthogonal to each other, $\boldsymbol{n}_1 = (1, -2, 1)/\sqrt{6}$ and $\boldsymbol{n}_2 = (1, 0, -1)/\sqrt{2}$. Then, denoting by (e_1, e_2, e_3) the components of $\boldsymbol{h}$ in the new basis, we have

$$e_1 = \frac{1}{\sqrt{6}}(h_1 - 2h_2 + h_3), \tag{38a}$$

$$e_2 = \frac{1}{\sqrt{2}}(h_1 - h_3), \tag{38b}$$

$$e_3 = \frac{1}{\sqrt{3}}(h_1 + h_2 + h_3) \tag{38c}$$

with

$$-\sqrt{\frac{2}{3}} \le \frac{e_1}{h} \le \frac{1}{\sqrt{6}}, \qquad -\frac{1}{\sqrt{2}} \le \frac{e_2}{h} \le \frac{1}{\sqrt{2}}, \qquad \frac{e_3}{h} = \frac{1}{\sqrt{3}}. \tag{39}$$

The map $(h_1, h_2, h_3) \mapsto (e_1, e_2, e_3)$ leads to $H_0 \mapsto \sqrt{3}e_3$, $\boldsymbol{\omega} \mapsto (0, 0, \sqrt{3})$, and $\boldsymbol{m} \mapsto (\mu_1, \mu_2, \mu_3)$ where

$$\mu_1 = \frac{1}{\sqrt{6}}(m_1\omega_1 - 2m_2\omega_2 + m_3\omega_3), \qquad \mu_2 = \frac{1}{\sqrt{2}}(m_1\omega_1 - m_3\omega_3),$$
$$\mu_3 = \frac{1}{\sqrt{3}}(m_1\omega_1 + m_2\omega_2 + m_3\omega_3). \tag{40}$$

Because of the resonance condition, it is always $\mu_3 = 0$. When $m_3 = 0$, we have $\mu_1 = \sqrt{3/2}m_1\omega_1^{\mathrm{r}}$ and $\mu_2 = m_1\omega_1^{\mathrm{r}}/\sqrt{2}$, while for null m_2 there results $\mu_1 = 0$ and $\mu_2 = \sqrt{2}m_1\omega_1^{\mathrm{r}}$. Unlike in the (h_1, h_2, h_3) representation, on M_h, the widths $(\Delta e_1)^{\mathrm{r}}_{\boldsymbol{m}}$ and $(\Delta e_2)^{\mathrm{r}}_{\boldsymbol{m}}$ are now different.

In Fig. 2 (left) we plot the solution of (24) for $|\boldsymbol{m}| \equiv |m_1| + |m_2| + |m_3| < 9$ after the transformation to M_h using (38a)–(38c). This figure displays the theoretical Arnold web, which is enclosed in a triangle of sides that, as already indicated in the figure, correspond to $h_3 = 0$ (upper side), $h_1 = 0$ (bottom side) and $h_2 = 0$ (side on the right). The vertices of such a triangle, $(1/\sqrt{6}, 1/\sqrt{2})$, $(-\sqrt{2/3}, 0)$, and $(1/\sqrt{6}, -1/\sqrt{2})$, correspond to periodic solutions of axis x, y and z, respectively. Those curves that are not straight lines have $m_1, m_2, m_3 \neq 0$ and are resonances of $\mathcal{O}(\epsilon^2)$, most of them appearing in $\mathcal{A}^0_{\epsilon^2}$ (with the appropriate signs in order to be a resonance). The theoretical Arnold web should look a bit different when actual motion is considered. Indeed, in such a case every curve should become a layer of finite width, as we illustrate in Fig. 2 (right). There we display, for a relatively large value of ϵ, the most relevant resonances at $\mathcal{O}(\epsilon)$ with their theoretical width given by (37) and transformed to (e_1, e_2) by recourse to (38a)–(38c).

3.1. Global dynamics by means of the MEGNO

Hamiltonian (17) depends, at first sight, on two parameters, namely, the energy h and ϵ. However, after rescaling the variables in the fashion $x_i \to \epsilon x_i$, $p_i \to \epsilon^2 p_i$ and $t \to t/\epsilon$, we have $\tilde{H} \to \epsilon^4\tilde{H} \equiv \bar{H}$, which is independent of ϵ, being thus the scaled energy, $\bar{h} = \epsilon^4 h$, the only free parameter. Then we allow ϵ to vary and fix the energy at the value $h = 1/(4\beta^4) \approx 0.485$. This adopted value for the energy leads to a period $T = 2\pi$ for the y, z-axial periodic orbits, which remain always stable despite the strength of the perturbation. The corresponding amplitudes of oscillation are $\beta^{-1} > 1$. For $\epsilon \neq 0$, the x-axial periodic orbit does not exist and it shows up, in general, as a chaotic orbit on the invariant plane $y = z$ or $h_2 = h_3$. However, there exist some stability intervals, for example, $\epsilon \lesssim 8 \times 10^{-4}$, $0.057 \lesssim \epsilon \lesssim 0.071$ and $0.073 \lesssim \epsilon \lesssim 0.076$, where both y and z oscillate, with the same frequency, about some negative value. This is shown in Fig. 3a where we display the final value of the MEGNO (after a rather

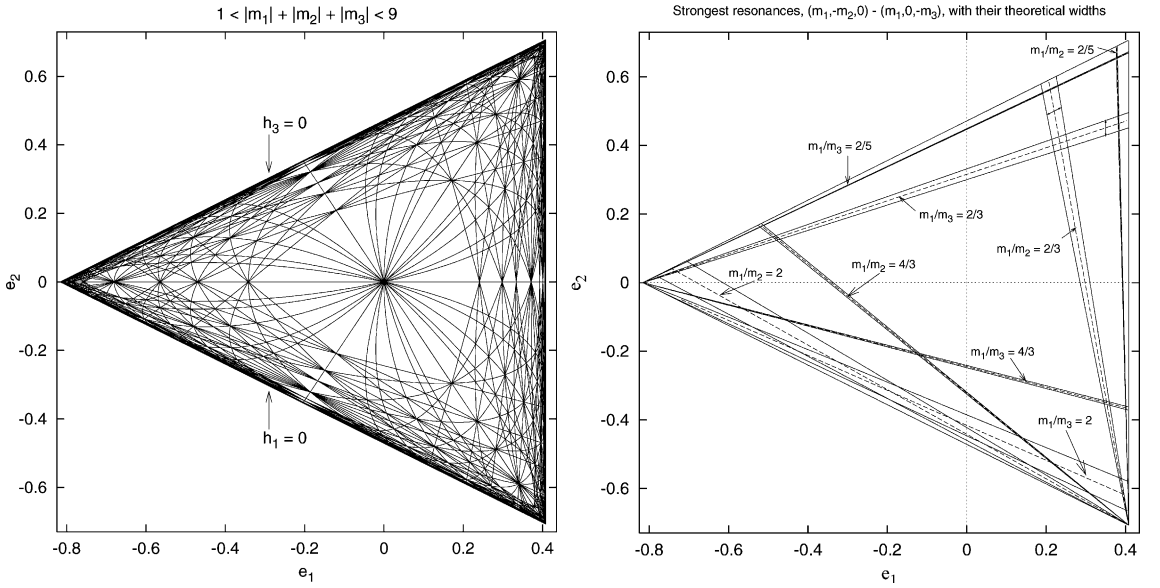

Fig. 2. Left: solution of the resonant polynomial (24) for $|\boldsymbol{m}| < 9\,(h = 1)$ yielding the theoretical Arnold web on the energy surface. Right: the strongest resonances and their width accordingly to (37)–(38c). Arrows within resonances $(2, -3, 0)$ and $(2, 0, -3)$ indicate the direction in which $\boldsymbol{\Delta h}^{\mathrm{r}}_{\boldsymbol{m}}$ oscillates about the corresponding resonant value.

long motion time) versus the perturbation parameter on $h_2 = h_3 = 0$. There we observe that over almost all the regarded interval, it is $\bar{Y} > 2$, indicating the unstable or chaotic character of the motion. Only within the above mentioned intervals, and in some other very narrow domains, do we get $\bar{Y} \leq 2$, revealing the existence of stable motion. In Fig. 3b we plot one stable orbit on the invariant plane $h_2 = h_3$, corresponding to $\epsilon = 0.06$.

Also the plane $(x, p_x) = (0, 0)$, or $h_1 = 0$, is invariant, as follows from the equations of motion for $\tilde{H}$, the remainder 2D Hamiltonian in (y, p_y, z, p_z) being integrable. The resulting motion is in general quasi-periodic, unless $h_2 = h_3$. Nevertheless, the normal variational equations to the x-motion at $h_1 = 0$ show that the motion could be either stable or unstable on $h_1 = 0$, as seen in Fig. 3c. There we plot, for $\epsilon = 0.005$, the value of the MEGNO after a certain motion time, t_f (see below), for 1000 orbits along the line $\hat{h}_2 + \hat{h}_3 = 1$, and we observe an unstable zone around the center.

For each adopted value of ϵ, we take values of h_1 and h_2 with $0 \leq h_1, h_2 \leq h$, $h_3 = h - h_1 - h_2$, being h_1 and h_2 of the form $jh/250$, $j = 0, \ldots, 250$. This leads to 31,626 initial conditions for which we take $(x, y, z) = (0, 0, 0)$. We integrate the equations of motion together with their first variationals over a total motion time $t_f = 3500T$. For the tangent vector, we adopt the initial values $\delta_x = \delta_y = \delta_z = 0$ and δ_{p_i} chosen at random in the interval $(-1, 1)$ and then normalized to 1. For each orbit we compute both $\bar{Y}(t_f)$ and the rate at which the MEGNO grows with time. When performing the least squares fit on $\bar{Y}(t)$ to obtain the LCN, only the last 80% of the time interval is considered in order to avoid the initial transient. The actual energies h_1, h_2, h_3, are scaled to the interval $[0, 1]$ (by division through h) and (38a)–(38c) are used to pass to the energy plane (e_1, e_2). We have considered 20 values of ϵ, ranging from 10^{-5} to 1, but only the most representative results concerning the global dynamics of the system are here enclosed.

In Figs. 4 and 5 we present the obtained values for $\bar{Y}(t_f)$ in a contour-like plot, for comparatively small and large values of ϵ, respectively. The values of $\bar{Y}(t_f)$ were binned in six intervals, one of them being very narrow and close to 2 (see figures for details). The gray-scale was simulated using different point sizes for different $\bar{Y}(t_f)$ intervals.

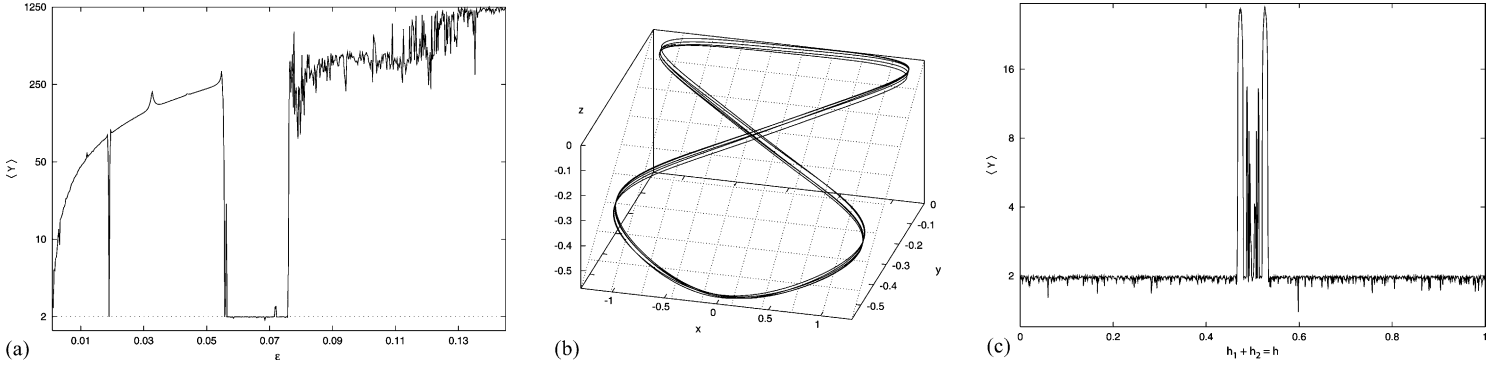

Fig. 3. (a) Plot of $\bar{Y}$ ($\langle Y\rangle$ in the figure) against ϵ on $h_2 = h_3 = 0$. (b) Stable orbit on the invariant plane $h_2 = h_3$ for $h_1 = h$, $h_2 = h_3 = 0$, $x_0 = 0$ and $\epsilon = 0.06$. (c) Values of $\bar{Y}$ ($\langle Y\rangle$ in the figure) on the invariant plane $h_1 = 0$ for $\epsilon = 0.005$ (see text).

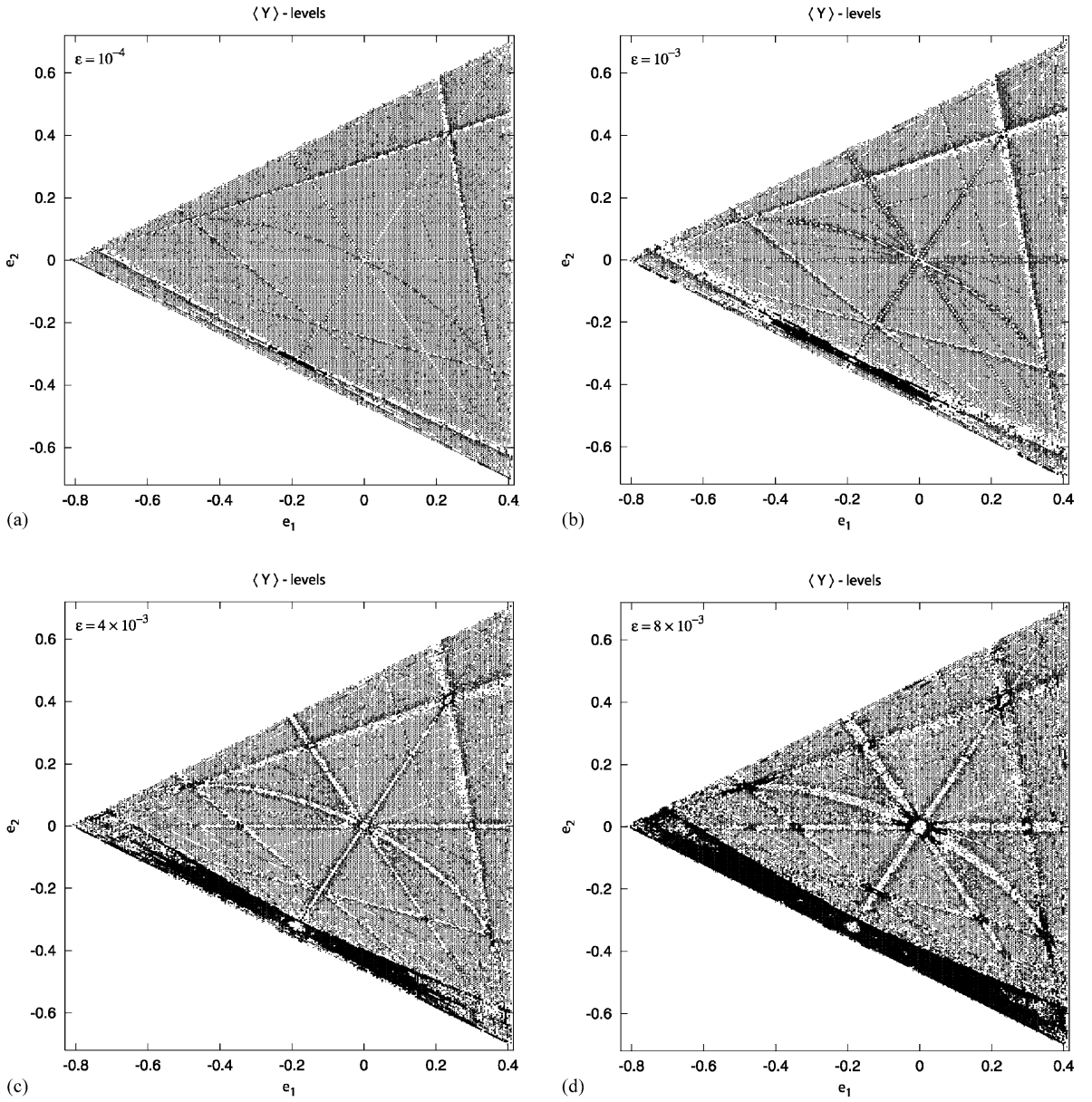

Fig. 4. $\bar{Y}(t_f)$-levels (indicated as $\langle Y \rangle$-levels in the picture) on the energy surface. The contour plot in gray scale (from white to dark-gray) corresponds to $\bar{Y}$ binned in six intervals: (a) [0, 1.9965), [1.9965, 1.9979), [1.9979, 2.1), [2.1, 3), [3, 10), [10,33); (b) [0, 1.9965), [1.9965, 1.998), [1.998, 2.1), [2.1, 3); [3, 15), [15, 98); (c) [0, 1.994), [1.994, 1.999), [1.999, 2.1), [2.1, 20), [20, 100), [100, 189); (d) [0, 1.991), [1.991, 1.999), [1.999, 2.1), [2.1, 10), [10, 55), [55, 251).

Let us say, however, that, in order to highlight some details at different perturbation values, the point sizes were not kept constant throughout all figures.

Fig. 4 exhibits most of the regular regime of the system. Indeed, Fig. 4a, which corresponds to the integrable model under a small perturbation, is in good agreement with what expected (see Fig. 2 (right) for comparison). All resonances in $\mathcal{A}^2_\epsilon$ as well as some in $\mathcal{A}^2_{\epsilon^2}$ can be clearly distinguished in the figure as light gray channels

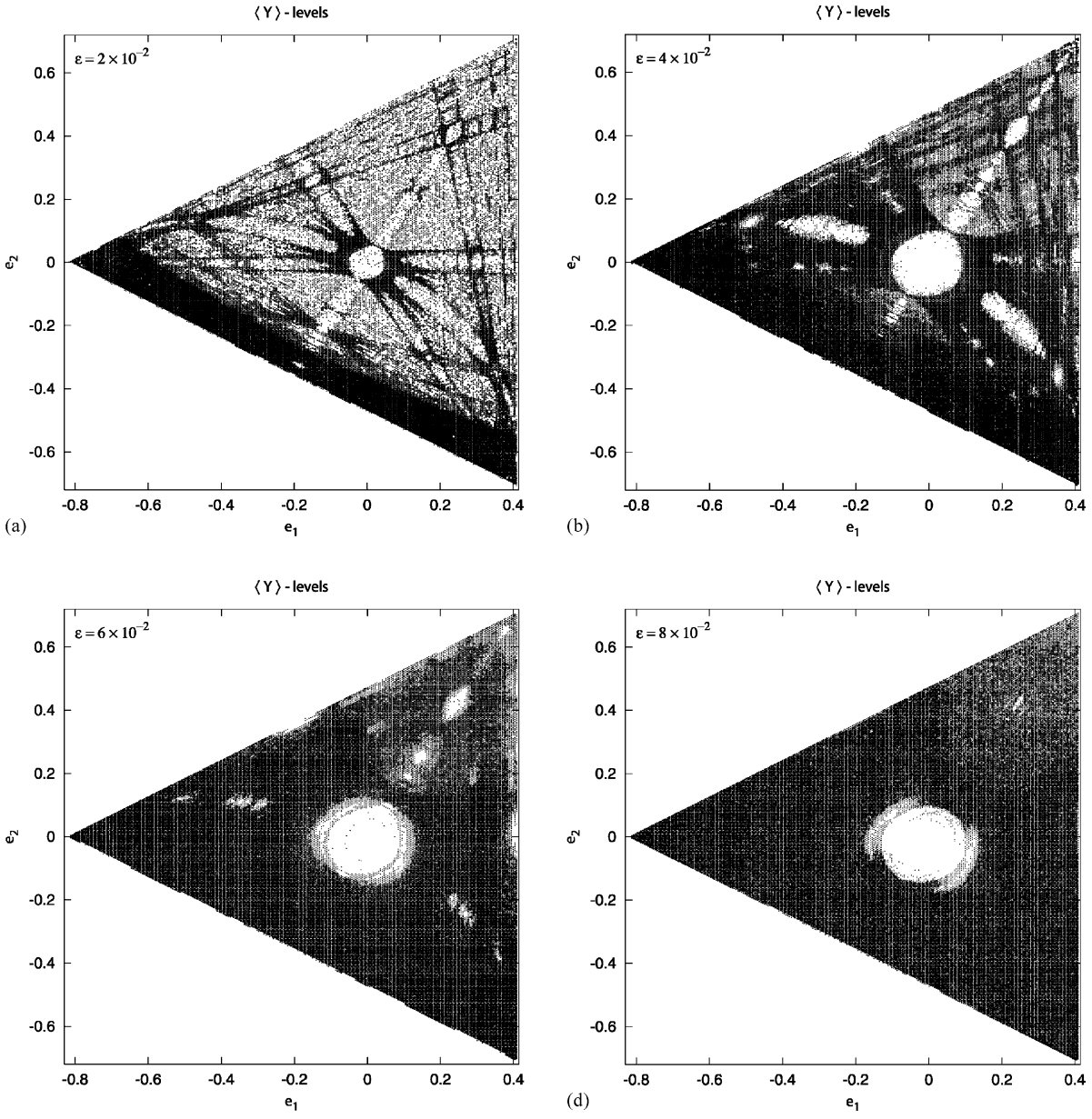

Fig. 5. $\bar{Y}(t_f)$-levels ($\langle Y \rangle$-levels in the figure) on the energy surface. The contour plot in gray scale (from white to dark-gray) corresponds to $\bar{Y}$ binned in six intervals: (a) [0, 1.993), [1.993, 2.005), [2.005, 5), [5, 45), [45, 150), [150, 383); (b) [0, 2.005), [2.005, 5), [5, 35), [35, 115), [115, 260), [260, 543); (c) [0, 2.005), [2.005, 30), [30, 100), [100, 200), [200, 350), [350, 738); (d) [0, 2.005), [2.005, 20), [20, 200), [200, 300), [300, 500), [500, 1026).

surrounded by dark boundaries. Thus, for instance, four resonances are seen to intersect at the origin, the three lines corresponding to the $(1, -1, 0)$, $(1, 0, -1)$, $(0, 1, -1)$ resonances and the curve being associated to the $(-2, 1, 1)$ resonance. Let us mention that the origin corresponds to exact energy equipartition, $h_1 = h_2 = h_3 = h/3$, which yields to a stable periodic orbit (see below). The global amount of stochasticity as a function of ϵ can be measured

by counting how many pixels have a value of $\bar{Y}(t_f)$ which exceeds some threshold. A convenient value is 1.998. Then, the fractions of stochasticity for the four values of ϵ in Fig. 4 are 5.8, 16.4, 32.6 and 44.3%, respectively. These figures do agree with a behaviour of the form $O(\sqrt{\epsilon})$.

As long as the perturbation is increased, resonances become wider. We can clearly distinguish their actual width as well as the narrow stochastic layers at their edges. The center of any resonance "channel" corresponds to a sequence of 2D elliptic tori while its borders (stochastic layer) to a sequence of 2D hyperbolic tori. Note that the MEGNO also reveals traces of many high-order resonances. As expected, for low values of ϵ, an important part of the energy surface is populated by 3D tori (quasi-periodic motion), while resonant motion (3D tori "trapped" in the resonances) occupies a small fraction of the phase space. For $\epsilon = 4$–8×10^{-3} (Fig. 4c and d), we observe a strip of chaotic motion close to $h_1 = 0$. The presence of this region is easily understood from Fig. 2, as the overlap of the strongest resonances, e.g. $(2, -1, 0)$ and $(2, 0, -1)$ as well as many others, for instance, $(4, -1, 0)$, $(4, 0, -1)$ and $(6, -1, 0)$, $(6, 0, -1)$ in $\mathcal{A}^2_\epsilon$ (not depicted in Fig. 2).

A quite interesting fact that MEGNO reveals is the common existence of stability zones at resonance intersections (also seen in Fig. 5). That is, when the system is at a multiple resonance. A chaotic domain should arise whenever two or more resonances cross. This occurs, in general, due to the intersections of the stable and unstable manifolds of the nearby related hyperbolic objects: either hyperbolic periodic orbits or center manifolds of elliptic–hyperbolic periodic orbits. But that domain can appear surrounding a stability region centered at a totally elliptic periodic orbit (intersection of at least two exact resonances). In Fig. 4d, for instance, deeply inside the chaotic zones near the center of the figure, we note a small stability "island" at the intersection of several resonances. Notice, however, that a change in the sign of some coupling term can produce a dramatic effect. This can be seen, for instance, at the lower right plot in Fig. 12, which should be compared with the upper right picture. This phenomenon is discussed in the last few paragraphs of Section 5.

Fig. 5 displays the dynamics at high-level perturbation, that is, the chaotic regime. There is some value of ϵ, near 5×10^{-2}, where a transition to, let us say, global stochasticity takes place. While for $\epsilon = 2 \times 10^{-2}$ a significant part of the energy surface still looks regular, with wide resonance domains and a broad chaotic strip (Fig. 5a), it looks very chaotic for a somewhat slightly larger perturbation (Fig. 5b). If, as done for Fig. 4, we fix a threshold $\bar{Y}(t_f) \leq 1.998$ to regard orbits as regular, the fractions of regular motion in the present figure are 38.3, 8.3, 5.7 and 4.9%, respectively, as we increase ϵ. Note, however, that within the weaker chaotic region, the MEGNO is still capable to unveil the relics of resonance structures. For larger perturbations (Fig. 5c and d), only the central zone and a few other small stability domains are present. Thus, while all these stability domains become smaller as ϵ increases, the one at the origin grows, about a factor 2, when ϵ goes from 2×10^{-2} to 4×10^{-2}, and then persists without significant changes up to $\epsilon \approx 0.1075$, when the central periodic orbit becomes unstable, the stability domain disappears and almost all the energy surface becomes completely chaotic.

Very similar pictures to those for $\bar{Y}(t_f)$ given in Figs. 4 and 5 are obtained when we plot the LCN, $\sigma_{\rm ls}$, derived by a least squares fit on $\bar{Y}(t)$ (see Fig. 6 corresponding to $\epsilon = 4 \times 10^{-2}$). Anyway, and since the MEGNO is a measure of hyperbolicity, a rough estimation of the positive LCN is also given by (see Eq. (14)) $\hat{\sigma}_1(t_f) = 2\bar{Y}(t_f)/t_f \sim 10^{-4}\bar{Y}(t_f)$. Indeed, taking, for instance, the value of the MEGNO corresponding to the center of the highest interval, $[260, 543)$, in Fig. 5b, we get $\log(\hat{\sigma}_1) \approx -1.437$, in agreement with the values $[-1.55, -1.3)$ corresponding to the highest interval in $\sigma_{\rm ls}$ in Fig. 6. On the other hand, the lowest values of $\log(\sigma_{\rm ls})$, ~ -7, are much smaller than those given by $\log(\hat{\sigma}_1)$, ~ -3.7. This shows that a least squares fit on $\bar{Y}(t)$ to get its time-rate is a very efficient procedure to separate stable and unstable motion in comparatively short times, as well as provide a good estimation of the positive LCN (see [7] for further details).

Turning back to Figs. 4 and 5, we observe that diffusion over the energy surface may occur. This is obvious in the case of large perturbations (Fig. 5c and d), but for smaller perturbations (Figs. 4c, d and 5 a, b) it looks like diffusion could take place along the chaotic layer of a given resonance and eventually spread over the whole

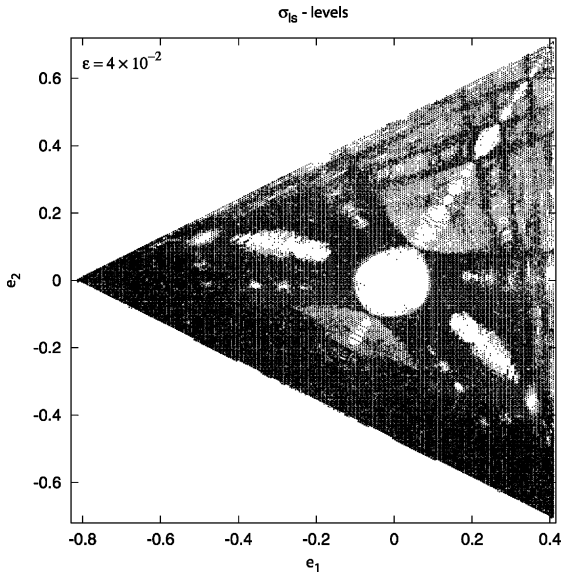

Fig. 6. $\log(\sigma_{\rm ls})$-levels ($\langle Y\rangle$-levels in the figure) on the energy surface. The contour plot in gray scale (from white to dark-gray) corresponds to $\log(\sigma_{\rm ls})$ binned in six intervals: $[-8.2, -4.2)$, $[-4.2, -2.55)$, $[-2.55, -2.25)$, $[-2.23, -1.78)$, $[-1.78, -1.55)$, $[-1.55, -1.3)$.

energy surface through the intersecting zones (this conjecture is usually quoted in physical literature as "Arnold diffusion"). However, as we show below, such intersections of resonances have a rather complicated structure and, instead of being a source where chaotic motion spreads, they could act as a barrier to diffusion. Let us mention that preliminary studies on diffusion on the energy surface at moderate-to-high perturbation ($\epsilon \sim 10^{-2}$) reveal that, for typical times $t_f \gtrsim 10^8 T$, "fast" diffusion only takes place on the chaotic strip close to $h_1 = 0$. But this is still a research in progress and will be the subject of a forthcoming work. For related experiments with symplectic maps we refer to [26].

In order to illustrate some details of the phase space structure at moderate perturbations, we present in Fig. 7a, a plot similar to those given in Figs. 4 and 5, but for $\epsilon = 5 \times 10^{-3}$ and with a higher resolution in h_1 and h_2 (step $10^{-3}h$ in both of them, that is, 501,501 orbits). In this plot we have skipped all points with $1.995 \le \bar{Y}(t_f) < 2$ (corresponding to quasi-periodic motion) in order the resonances be distinguished more clearly. Near 76% of the pixels correspond to $\bar{Y}(t_f) < 2$ and the number of pixels exceeding the value 1.998 is slightly below 37% (compare with the data for Figs. 4 and 5).

Note the complexity of the picture shown in Fig. 7b, where we present a zoom around the intersection of resonances at the origin. The contour plot was obtained with a higher resolution in h_1 and h_2 (step $10^{-4}h$ in both of them) and for a total motion time $t_f = 350T$. There the MEGNO reveals the existence of several stability zones, which should be responsible for restraining the spread of chaotic motion, acting in the manner of barriers to diffusion. They are the sticky tori surrounding the periodic orbit located at the center of the resonance. This plot is also very illustrative to see how the manifolds of lower-dimensional tori bend in a complex fashion, giving rise to the many tight loops seen in the picture. These manifolds are important because they are the objects able to carry the motion arriving along one of the resonances either to the "other part" of the resonance or to a different resonance.

Further details of the resonance structure are shown in Fig. 7c, where a zoom along a thin resonance channel is displayed. For this contour plot the initial conditions were taken spanning h_1 and h_2 intervals, so that the rectangle appears distorted because of the transformation to the (e_1, e_2)-plane. Again the total motion time considered is $t_f = 350T$ and the same magnification (step $10^{-4}h$ as in (b)) has been used.

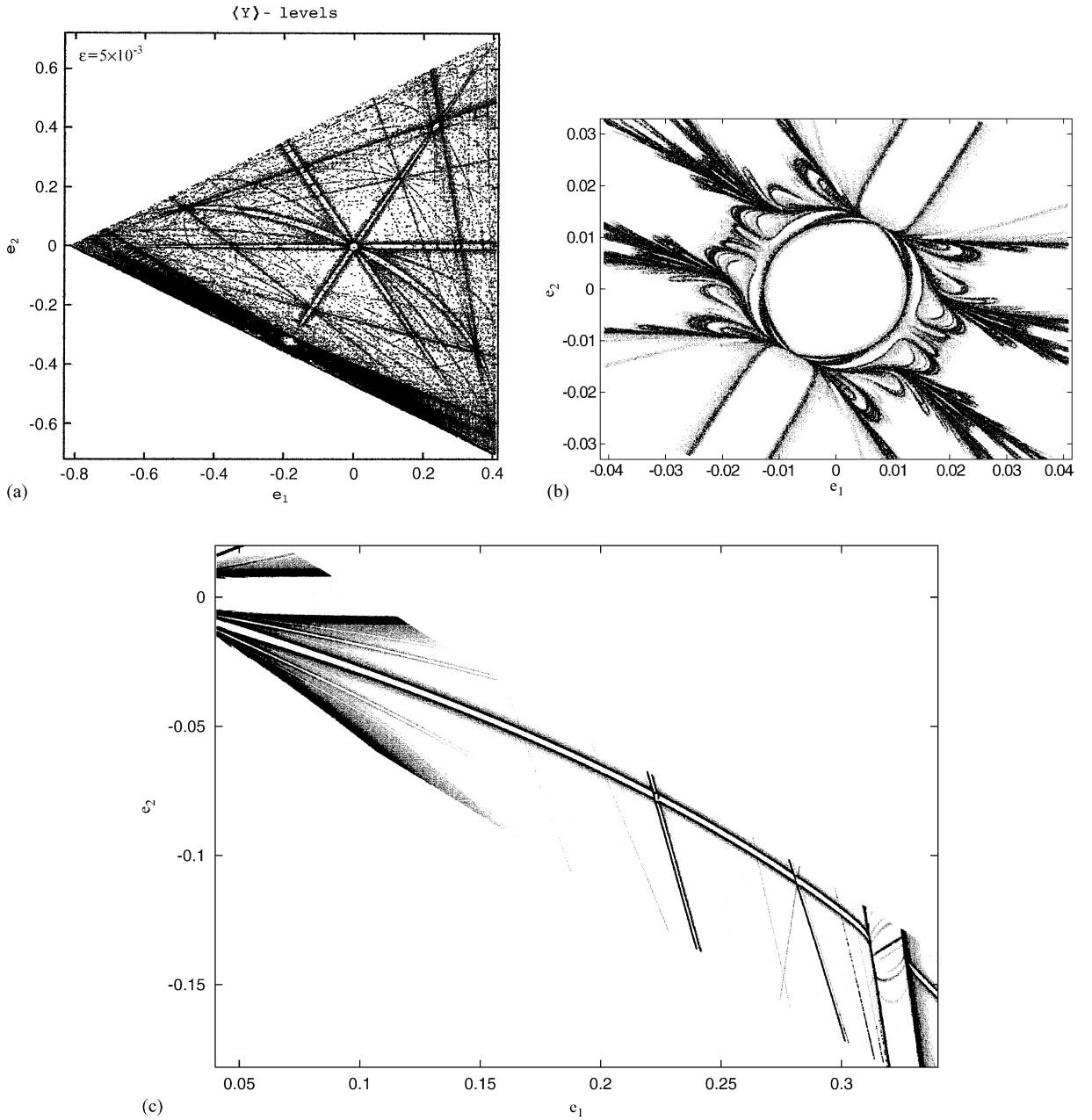

Fig. 7. $\bar{Y}(t_f)$-levels on the energy surface for $\epsilon = 5 \times 10^{-3}$ (a); zoom around $(e_1, e_2) = (0, 0)$ (b); zoom along a thin resonance channel (c). The contour plots correspond to $\bar{Y}$ binned in the intervals: (a) [1.99, 1.995), [2, 2.015), [2.015, 20), [20, 160), [160, 215); (b) [2.15, 2.6), [2.6, 8); (c) [1.969, 1.978), [2.008, 2.11), [2.11, 9). In (a), $t_f = 3{,}500T$ while in both (b) and (c), $t_f = 350T$.

A few data on the computational cost of the preceding figures can be relevant. For these computations an array of processors (HIDRA) has been used. At the time the computations were done, it consisted of 42 dual PC, most of them Pentium at 500 MHz running under Linux. For each one of the plots in Figs. 4 and 5 the CPU time was slightly less than 2 h, while Fig. 7a took 34 h.

Let us notice that similar resonance structures were obtained via Laskar's frequency mapping technique when applied to the dynamical study of triaxial galactic models (see [23,28]). These resonance structures, though resembling the ones shown above, are far less detailed, so hiding relevant dynamical information.

4. Generalization of the MEGNO

As we have already shown in the example above, the MEGNO does succeed in providing a clear indication of regular and chaotic behaviour as well as in producing good estimates of the LCN. Let us though generalize the MEGNO in the following fashion:

$$Y_{m,n}(\gamma(t)) = (m+1)t^n \int_0^t \frac{\dot{\delta}(\gamma(t'))}{\delta(\gamma(t'))}(t')^m \, \mathrm{d}t', \tag{41}$$

now defining

$$\bar{Y}_{m,n}(\gamma(t)) = \frac{1}{t^{m+n+1}} \int_0^t Y_{m,n}(\gamma_q(t')) \, \mathrm{d}t' \tag{42}$$

and analyze whether any benefit would turn out when taking values for the exponents (m, n), $m \geq 0$ other than the natural choice $(1, -1)$ which yielded (6) and (10). Note also that $Y_{m,n}$ with the choice $(0, -1)$ gives, in the limit when $t \to \infty$, the value of σ as defined in (4).

The time evolution of $Y_{m,n}$ in case of regular, quasi-periodic motion, is given by the expression:

$$Y_{m,n}(\gamma_q(t)) \approx (m+1)\left(\sum_{k=0}^{m-1} \frac{(-1)^k t^{m+n-k}}{(m-k)\lambda_q^k} + (-1)^m \frac{t^n \, \ln(1+\lambda_q t)}{\lambda_q^m}\right) + O(\gamma_q(t)), \tag{43}$$

which obviously reduces to (9) for $(m, n) = (1, -1)$. Then, for t large enough we get

$$\frac{Y_{m,n}(\gamma_q(t))}{t^{m+n}} \approx \frac{m+1}{m}, \tag{44}$$

so the quotient $Y_{m,n}/t^{m+n}$ saturates to a constant value as $t \to \infty$. Moreover, from both (42) and (43) it follows that

$$\bar{Y}_{m,n}(\gamma_q(t)) \approx \frac{m+1}{m(m+n+1)}, \quad t \to \infty, \tag{45}$$

which is also a fixed constant not depending on the orbit.

In the case of an irregular orbit, γ_i, of LCN σ_i, we have

$$\frac{Y_{m,n}(\gamma_\mathrm{i}(t))}{t^{m+n}} \approx \sigma_i t + \tilde{O}(\gamma_\mathrm{i}(t)), \tag{46}$$

while, on considering a sufficiently large time, we obtain

$$\bar{Y}_{m,n}(\gamma_\mathrm{i}(t)) \approx \frac{\sigma_i t}{m+n+2}. \tag{47}$$

For a chaotic orbit then, both $Y_{m,n}/t^{m+n}$ and $\bar{Y}_{m,n}$ grow linearly with time, at a rate that is proportional to the LCN of the orbit.

Therefore, the asymptotic behaviour of $\bar{Y}_{m,n}$ can still be recast as $\bar{Y}_{m,n}(\gamma(t)) \approx a_\gamma t + d_\gamma$, where now $a_\gamma = \sigma_i/(m+n+2)$ and $d_\gamma \approx 0$ for irregular, stochastic motion, while $a_\gamma = 0$ and $d_\gamma \approx (m+1)/m(m+n+1)$ for stable, quasi-periodic motion.

Further, as it turns out from Eqs. (45) and (47), the LCN can also be recovered by a simple linear least squares fit on $\bar{Y}_{m,n}(\gamma(t))$.

Let us notice that the quantity $\hat{\sigma}_{1,m,n} = Y_{m,n}/t^{m+n+1}$ verifies

$$\hat{\sigma}_{1,m,n}(\gamma_q(t)) \approx \frac{m+1}{mt}, \qquad \hat{\sigma}_{1,m,n}(\gamma_i(t)) \approx \sigma_i, \quad t \to \infty, \tag{48}$$

which show that, in case of regular motion, $\hat{\sigma}_{1,m,n}$ also converges to 0 faster than σ_1 that goes as $\ln t/t$, while for chaotic motion, both magnitudes approach the positive LCN at a rather similar rate. Notice that the asymptotic behaviour of $\hat{\sigma}_{1,m,n}$ in the regular regime does not depend on the exponent n.

From the several experiments carried out taking different values for the exponents, it looks like the larger m, the faster the convergence of $\bar{Y}_{m,n}$ to a constant value in case of regular motion. Nonetheless, for m rather large, it seems to play a role the total time considered, as the effect of the latter points is reinforced giving rise to somewhat small oscillations.

An exhaustive comparison of the MEGNO(m, n)'s performance for different exponents (m, n) revealed that, besides the natural choice $(1, -1)$, also the values $(2, 0)$ serve to distinguish regular from chaotic behaviour in a quite efficient manner (see below).

Just for the sake of illustration, let us turn back to the 2D Hénon–Heiles example given in Section 2. For the same three regular orbits there labeled as (sp), (qp) and (up), we computed both $Y_{m,n}$ and $\bar{Y}_{m,n}$, by means of (41) and (42), respectively, for three different choices of (m, n), namely, $(1, -1)$, $(2, 0)$ and $(3, 1)$.

In Fig. 8 we show that in case of regular motion, $\bar{Y}_{m,n}$ evolves with time as predicted by Eq. (45). Indeed, the temporal evolution of $\bar{Y}_{m,n}$ for all the three regular orbits is seen to tend to the asymptotic values 2, $1/2$ and $4/15$,

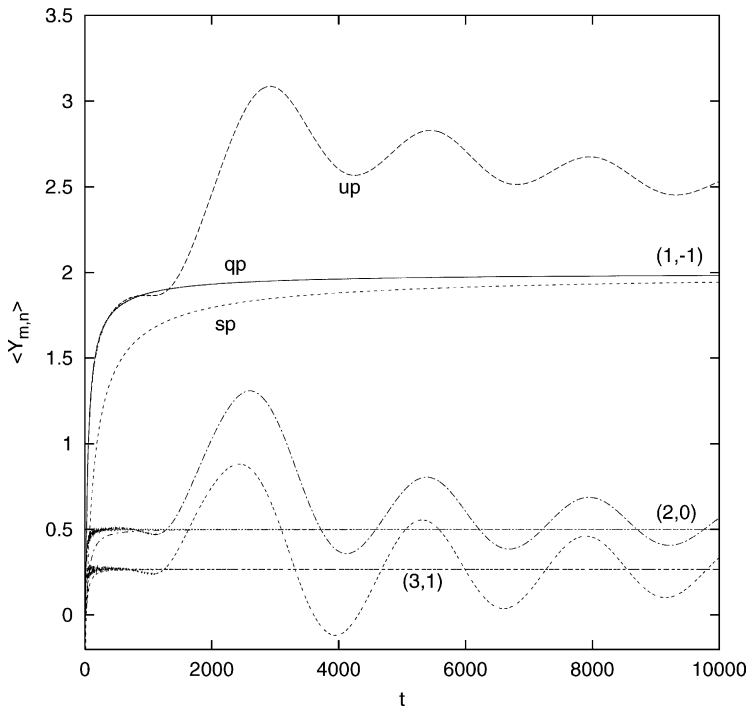

Fig. 8. Time evolution of $\bar{Y}_{m,n}$ ($\langle Y\rangle_{m,n}$ in the plot) for the regular orbits (sp), (qp) and (up) in the Hénon–Heiles model, for different values of the exponents (m, n).

when the exponents are $(1, -1)$, $(2, 0)$ and $(3, 1)$, respectively. We observe that, for the stable quasi-periodic orbit (qp), $\bar{Y}_{m,n}$ rapidly converges to the value given in (45), a faster convergence being observed the larger is m. Also for the orbit close to a stable periodic one, (sp), does $\bar{Y}_{m,n}$ reach the constant value (45) faster as a greater m is considered. Meanwhile, for the trajectory close to an unstable periodic orbit, (up), smaller oscillations around the asymptotic value (45) do show when $m = 2$.

From the comparison we conclude that the MEGNO (2, 0) allows for clearly separating the regular and chaotic regime even in rather short motion times. Furthermore, if we use the quantity $4\bar{Y}_{2,0}$, we see that for regular orbits it tends to 2, as $\bar{Y}_{1,-1}$ does, while for orbits with exponential instability it tends to behave as $\sigma_i t$. Then, either a linear fit or simply $4\bar{Y}_{2,0}(\gamma_i(t))/t$ supplies an estimate of the LCN. However, the choice $(1, -1)$ for the exponents offers the additional benefit of more clearly identifying stable and unstable periodic motion as well.

5. The MEGNO for maps

In this section we show how this numerical tool applies to discrete dynamical systems. For dealing with maps, the MEGNO is defined essentially as before, but summing over the iterates of the map instead of integrating with respect to t, and taking the differential map in place of the variational equations.

For a given initial point Q_0, iterates under a given map P are to be computed yielding points $Q_k = P^k(Q_0)$. An initial "random" tangent vector v_0, $\|v_0\| = 1$, is transported under the differential map DP, to obtain vectors $v_k = DP^k(Q_0)v_0$. Then, after N iterates, the MEGNO is computed by means of

$$Y_{m,n}(N) = (m+1)N^n \sum_{k=1}^{N} \ln\left(\frac{\|v_k\|}{\|v_{k-1}\|}\right) k^m \tag{49}$$

and

$$\bar{Y}_{m,n}(N) = \frac{1}{N^{m+n+1}} \sum_{k=1}^{N} Y_{m,n}(k). \tag{50}$$

The algorithm has been tested with different values for the exponents m and n. Again, it turned out that the larger m, the faster $\bar{Y}_{m,n}$ converges to a constant value for regular motion, but, for m rather large, small oscillations show up. However, the bumpy late evolution of $\bar{Y}_{m,n}$ (which is also present in the continuous case, as Fig. 8 shows, in the case of (up) orbits) is diminished if the iteration is stopped when the distance between the initial and final points is minimum ("right-stop" condition). On returning close to the initial point, the effect of the periodic or quasi-periodic oscillations added to a regular behavior is minimized. This sort of refinement in regards to the stop time, has proven rather efficient in smoothing such oscillations.

For the sake of illustration, two examples are included where the values (2, 0) have been adopted for the exponents. This choice, together with the "right-stop" condition, has shown to provide a fairly good fast indicator, the MEGNO (2, 0)rs. A minor additional modification is also convenient with the choice $(m, n) = (2, 0)$. Let us define the quantity

$$\hat{Y}_{2,0}(N) = \frac{4\bar{Y}_{2,0}(N) - 2}{N}, \tag{51}$$

which tends to 0 in the regular case and to σ_i in the case of an irregular orbit. Negative values of $\hat{Y}_{2,0}(N)$ appear for regular orbits (provided N is taken not too small), while small positive values identify mild chaos. The resolution can eventually be improved by means of a linear fit of $4\bar{Y}_{2,0}(N) - 2$, but in the forthcoming examples we have used simply (51) with the rs criterion.

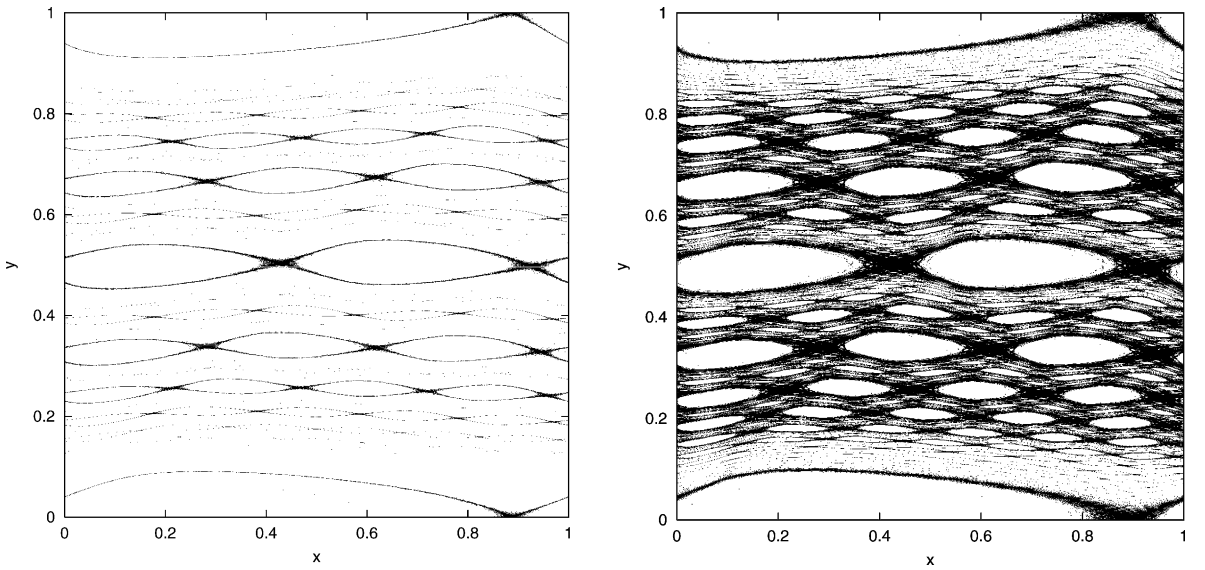

Fig. 9. $\hat{Y}_{2,0}$-levels for the RSSM (see text) corresponding to $\mu = 0.8$ (left) and $\mu = 0.85$ (right). Regions of regular behaviour are depicted in white and those of chaotic behaviour in black.

5.1. Examples

Let us first be concerned with the rational shifted standard map (see [12] for details). This is a 2D area-preserving discrete dynamical system given by the equations:

$$y' = y + \epsilon f(x), \qquad x' = x + \epsilon y \tag{52}$$

with $x \in [0, 2\pi)$, $y \in [0, 2\pi/\epsilon)$, and where

$$f(x) = \frac{\sin(x+\varphi)}{1-\mu\cos x} - \Delta, \quad \Delta = \frac{\mu}{\sqrt{1-\mu^2}+1-\mu^2}. \tag{53}$$

Notice that (52) and (53) define a standard map modified in order to have a no longer symmetric nor entire function f. Indeed, symmetry is lost through the introduction of the phase φ, while the parameter $\mu \in [0, 1)$ breaks the entire character of f. The quantity Δ is fixed so that f has zero average.

The MEGNO (2, 0)rs has been applied to (52) in an equispaced grid of 1000×1000 pixels in the domain $(x/2\pi, y\epsilon/2\pi) \in [0, 1) \times [0, 1)$, for a sample of $\mu \in [0, 1)$. A maximum of N iterates has been computed, for $10{,}000 < N < 11{,}000$, the iteration being stopped when the distance $|P^N(Q_0) - Q_0|$ is minimum, according to the "right-stop" condition. The results for $\mu = 0.8$ and $\mu = 0.85$ are presented in Fig. 9, where we have adopted the values $\epsilon = 0.2$ and $\varphi = 1$ for the remaining parameters. There the pixels corresponding to initial conditions of regular behaviour have been plotted in white and those of chaotic behaviour in black. While for $\mu = 0.8$ the regular regime prevails (plot on the left), the dynamics for $\mu = 0.85$ displays many chaotic components (plot on the right), but rotational invariant curves (joining the vertical boundaries) still exist. Note that the variation of μ has been small, but the effects are quite dramatic. A small additional increase in μ produces the destruction of all these curves and a large chaotic zone appears. Notice that the MEGNO (2,0)rs also succeeds in unveiling the resonance structure of the system.

Fig. 10 illustrates the application of the MEGNO to describe the regular or chaotic behaviour for fixed values of μ. In each 1000×1000 pixels plot values of $\epsilon \in [0.001, 1]$ (vertical axes) have been used, and as initial conditions

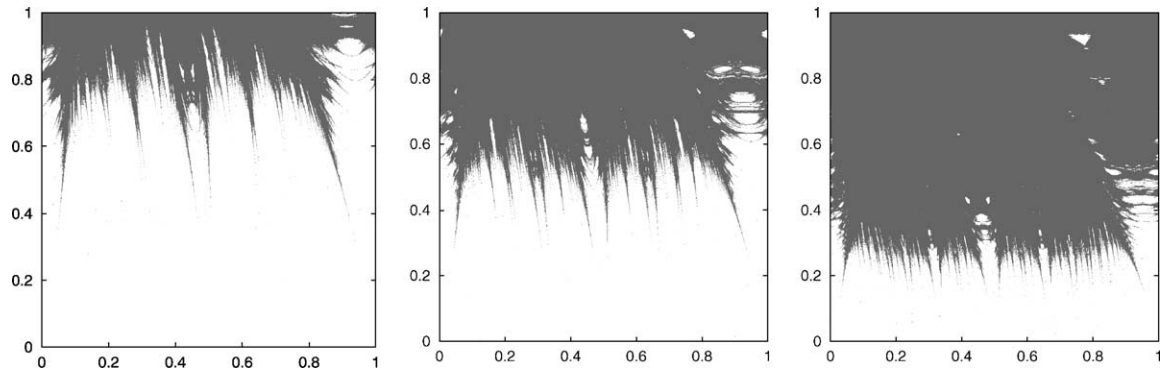

Fig. 10. The chaotic regions of the RSSM for different values of μ. From left to right the values of $\mu = 0.4, 0.6$ and 0.8 have been used. On the vertical axis we display ϵ while the horizontal one contains the initial value of $y\epsilon/2\pi$. The initial value of x has been taken equal to 0 in all cases. Dark-gray pixels correspond to chaotic motion.

$x = 0$ and $y\epsilon/2\pi \in [0, 0.999]$ (horizontal axes). The parameter φ is kept equal to 1 in all cases. The chaotic behaviour at the boundaries of the resonant zones (where the islands are present) can be clearly seen, as well as their evolution with μ. We refer to [12] for the analysis of the RSSM using FMA. The frequency analysis provides information on the rotation numbers of the invariant curves, but the computational cost to correctly discriminate the character of most of the pixels is much higher. Using $\hat{Y}_{2,0,\mathrm{rs}}$ the computing time on HIDRA for each plot in Figs. 9 and 10 is less than 3 min.

A comparison with the FLI is also instructive. We consider the RSSM for $\mu = 0.5, \varphi = 1$. To determine how reliable a method is to decide about the regular or chaotic character of the orbit corresponding to some initial conditions we have, first, set up a criterion. To this end, we have computed the maximal amplification of the length of a random initial vector for a maximum of $N = 10^6$ iterates. A threshold equal to $L = 10^{24}$ has been selected. Conditions exceeding L before N iterates are considered as chaotic. Otherwise, they are assumed to be regular. Several independent tests have been used to rely on the results (see [1] for tests to decide whether a point is on an invariant curve). Having assigned a character to each one of the 1000×1000 pixels with ϵ and $y\epsilon/2\pi$ as above, we have computed $N\hat{Y}_{2,0,\mathrm{rs}}(N)$ and the amplification factor A after N iterates, using $N = 10^4$ and $N = 2 \times 10^4$ in both cases. In the MEGNO approach the last 10^3 iterates have been used to select the best final point. Fig. 11 shows the number of "discrepancies", i.e. incorrect identifications among the 10^6 pixels. The horizontal variable denotes the value of the parameter used as an estimation of $\sigma_i N$ (either $N\hat{Y}_{2,0,\mathrm{rs}}(N)$ or A). The dots are located at the respective minima of the number of discrepancies. They are 1878 and 975 for the MEGNO estimates and 3209 and 1852 using A at the end of each run. It follows that with the same effort (and even without using a fitting) the MEGNO reduces the number of discrepancies by a factor around 1.8 and furthermore, the value of σ_i where the minimum is found is much closer to 0, as it should be (1.50×10^{-4} and 0.95×10^{-4} against 5.18×10^{-4} and 2.90×10^{-4}, respectively). Several other choices of (m, n)rs have been tested, modifying the numerator in (51) to $(m + n + 2)(\bar{Y}_{m,n}(N) - (m + 1)/m(m + n + 1))$. The results are similar for different couples like $(m, n) = (2, 0), (2, 1), (2, 2), (3, -2), (3, -1)$ and, among them, $(2, 0)$ seems to be the simplest one.

Let us now turn to a 4D conservative map, the coupled rational shifted standard map, consisting of two coupled rational shifted standard maps so that it is described by the equations:

$$
\begin{aligned}
y_1' &= y_1 + \epsilon_1 f_1(x_1) + \gamma_+ f_3(x_1 + x_2) + \gamma_- f_3(x_1 - x_2),\\
y_2' &= y_2 + \epsilon_2 f_2(x_2) + \gamma_+ f_3(x_1 + x_2) - \gamma_- f_3(x_1 - x_2),\\
x_1' &= x_1 + \epsilon_1 y_1, \qquad x_2' = x_2 + \epsilon_2 y_2
\end{aligned}
\tag{54}
$$

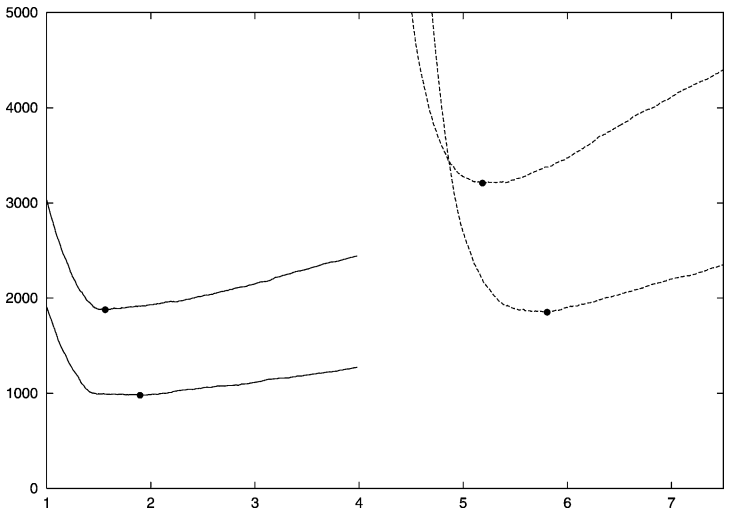

Fig. 11. Number of discrepancies as a function of the estimator of $\sigma_i N$ using MEGNO (2, 0)rs (curves on the left) and the usual Lyapunov estimator (curves on the right). The upper curves correspond to $N = 10^4$ and the lower ones to $N = 2 \times 10^4$.

with $x_i \in [0, 2\pi)$, $y_i \in [0, 2\pi/\epsilon_i)$, $i = 1, 2$, and where

$$f_i(x) = \frac{\sin(x + \varphi_i)}{1 - \mu_i \cos x} - \Delta_i, \quad \Delta_i = \frac{\mu_i}{\sqrt{1 - \mu_i^2} + 1 - \mu_i^2}, \quad i = 1, 3 \tag{55}$$

with $\mu_i \in [0, 1)$, and the quantities Δ_i so fixed that f_i have zero average. Notice that two coupling terms in $(x_1 + x_2)$ and $(x_1 - x_2)$ have been added, γ_+ and γ_- being the coupling parameters.

Several experiments have been carried out using different values for the parameters. The algorithm MEGNO (2, 0)rs has been applied to an equispaced grid of 1000×1000 pixels in the domain $(y_1\epsilon_1/2\pi, y_2\epsilon_2/2\pi) \in [0, 1) \times [0, 1)$. The initial values for the remaining variables are $x_1 = 0$, $x_2 = 0$. The "right-stop" condition has been applied, so that for each initial condition the iteration is stopped after N iterates, $10{,}000 < N < 11{,}000$, when the distance $|P^N(Q_0) - Q_0|$ is minimum.

Since we have come here to a problem of higher dimension, we have to compute the iterates under *DP* of two "random" initial vectors v_{10}, v_{20}, $\|v_{i0}\| = 1$, which we orthogonalize and renormalize at each iterate. The MEGNO associated with each direction is computed and the maximum of the two is used in order to determine the character of the trajectory. The results corresponding to $\mu_1 = 0.5$, $\varphi_1 = 1$, $\mu_2 = 0.4$, $\varphi_2 = 2$, $\mu_3 = 0.6$, $\varphi_3 = 3$ are displayed in Fig. 12 for $\epsilon_1 = 0.1$, $\epsilon_2 = 0.2$, and different values of the coupling parameters γ_+ and γ_-, which are indicated on top of each plot. The lower right plot has the same values of γ_+ and γ_- on top of it, but the parameter ϵ_2 is now negative. The fact that in the coupling we face to an indefinite form rather than a positive definite one produces a dramatic effect on the resonances. The contour-like plots in gray scale (from white to dark-gray) exhibit the obtained values for $\hat{Y}_{2,0,\mathrm{rs}}$ binned in three intervals. The orbits such that $\hat{Y}_{2,0,\mathrm{rs}}(N) < 0.01$ have been selected as regular, while those with $\hat{Y}_{2,0,\mathrm{rs}}(N) > 1$ are considered chaotic. The intermediate range is regarded as, possibly, mildly chaotic.

A resonance can be identified again as a light gray channel surrounded by dark boundaries. If it is thin perhaps only some trace of the light and/or dark-gray can be seen. Hundreds of resonances can be detected in Fig. 12. The resonances in the vertical and horizontal directions are present even if $\gamma_\pm = 0$ and their amplitudes depend, essentially, on $|\epsilon_j|$, $j = 1, 2$. As long as the coupling parameters are increased, resonances are seen to become wider, their actual width as well as their narrow stochastic layers at their edges being clearly distinguished. Further details on the CRSSM dynamics may be found in [26].

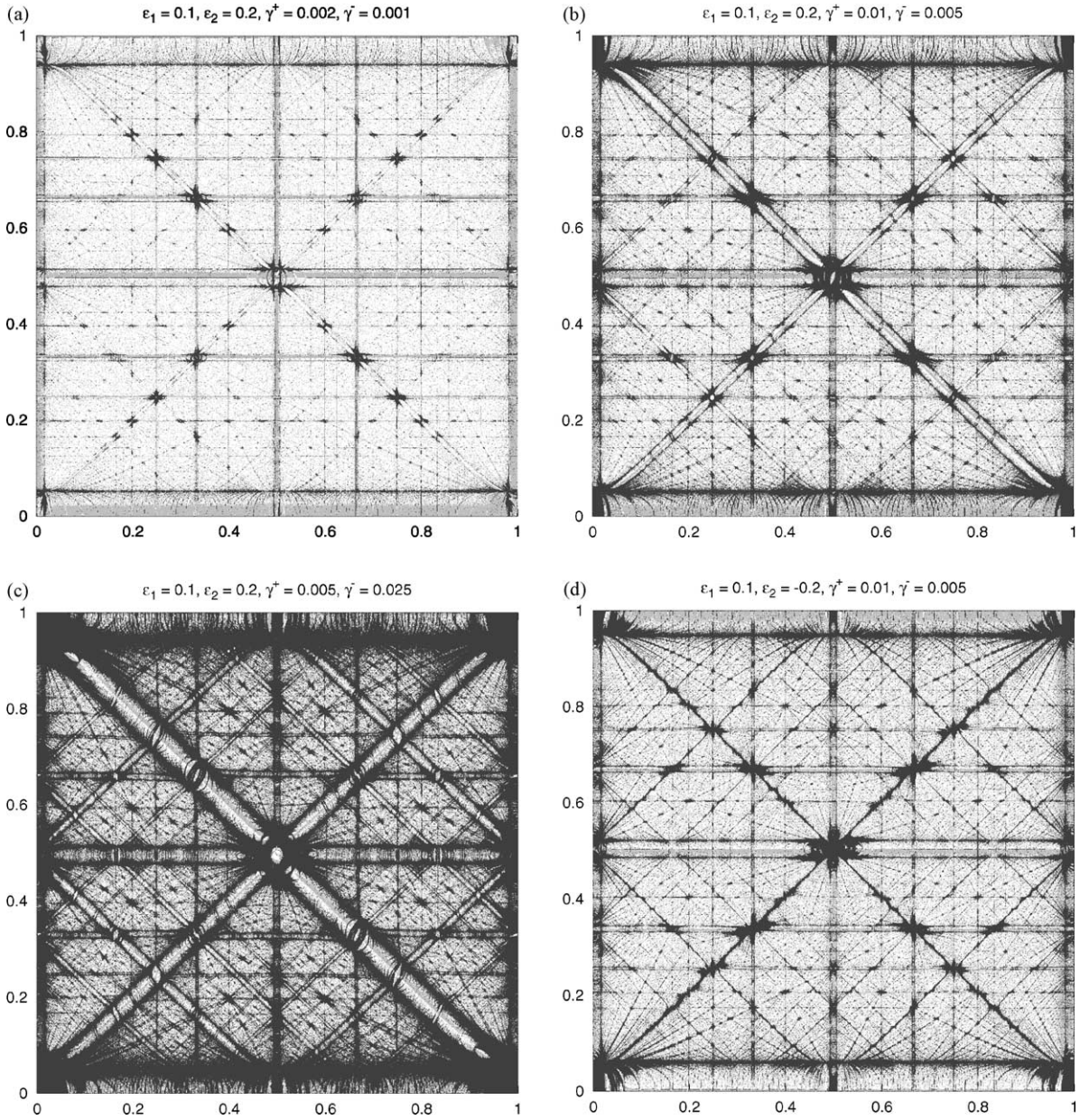

Fig. 12. $\hat{Y}_{2,0}$-levels for the CRSSM for different values of the coupling parameters γ_+ and γ_-. The contour plots in gray scale (from white to dark-gray) correspond to $\hat{Y}_{2,0}$ binned in three intervals; pixels corresponding to initial conditions of regular behaviour are plotted in white, and those of chaotic behaviour in dark-gray.

6. Conclusions

In this paper we have shown how a rather simple technique, like the MEGNO, succeeds in providing detailed indications on the global dynamics of Hamiltonian systems and maps.

This technique furnishes an efficient algorithm that allows not only to clearly identify regular and irregular motion as well as stable and unstable periodic orbits, but also to obtain a quite good estimate of the LCN in comparatively short motion times, for both ordered and stochastic components of phase space. Thus, by the application of a single tool it is possible to grasp the global dynamics of the system, this procedure being a first attempt to get dynamical information about the motion using the whole orbit.

Here we have presented numerical evidence of the MEGNO being a fast indicator capable of unveiling the hyperbolic structure of the phase space, as well as yielding a clear picture of the resonance structure, even in the case of multi-dimensional systems, which are not easy to be dealt with. The MEGNO is shown to provide the actual size of a resonance as well as reveal its internal structure.

The algorithm has been applied to a 3D perturbed quartic oscillator. A quite interesting result is the existence of stability zones in almost all resonance intersections. Indeed, in this case a chaotic domain is seen to show up whenever two or more resonances intersect, but always surrounding a stability region centered at a stable periodic orbit. Diffusion over the energy surface may occur, which is obvious for large perturbations, but in case of smaller perturbations, the MEGNO elucidates such a complex structure of the resonance intersections, that they could restrain the spreading of chaotic motion.

Further results regarding diffusion on the energy surface at moderate-to-high perturbation will be the subject of forthcoming papers.

Also has the MEGNO's performance when applied to conservative maps been illustrated by its application to both the 2D rational shifted standard map and the 4D coupled rational shifted standard map. There this technique has demonstrated its efficiency as a fast and reliable method to estimate the main dynamical features and their significance when dealing with discrete dynamical systems.

Acknowledgements

The authors thank A. Maciejewski for making available the references [13,14]. PMC and CMG would like to acknowledge CONICET (Argentina) for financial support through the *Instituto de Astrofísica de La Plata*. The research of CS has been supported by grants DGICYT BFM2000-805 (Spain) and CIRIT 2000 SGR-27 (Catalonia). Partial support of grant INTAS 2000-221 is also acknowledged. An extensive use of HIDRA (UB), an array of 42 dual PC, has been made. We are grateful to CIRIT, DGICYT and the University of Barcelona who are providing funds for this array of processors.

References

[1] H.W. Broer, I. Hoveijn, M. van Noort, C. Simó, G. Vegter, The parametrically forced pendulum: a case study in $1+1/2$ degrees of freedom, Preprint, 2001.
[2] H.W. Broer, C. Simó, Bul. Soc. Bras. Mat. 29 (1998) 253.
[3] H.W. Broer, C. Simó, J.C. Tatjer, Nonlinearity 11 (1998) 667.
[4] H.W. Broer, C. Simó, R. Vitolo, Nonlinearity 15 (2002) 1.
[5] B. Chirikov, Phys. Rep. 52 (1979) 263.
[6] P. Cincotta, C. Giordano, in: O.C. Winter, A.F. Bertachini, A. Prado (Eds.), Advances in Space Dynamics 2: Applications in Astronomy, Sao Jose dos Campos, 2002, p. 237.
[7] P. Cincotta, C. Simó, Astron. Astrophys. Sup. 147 (2000) 205.
[8] P. Cincotta, C. Simó, in: V.G. Gurzadyan, R. Ruffini (Eds.), The Chaotic Universe. Advanced Series in Astrophysics and Cosmology, vol. 10, World Scientific, Singapore, 2000, p. 247.
[9] C. Froeschlé, E. Lega, R. Gonczi, Celest. Mech. Dynam. Astron. 67 (1997) 41.
[10] C. Froeschlé, M. Guzzo, E. Lega, in: B. Steves, A. Maciejewski (Eds.), The Restless Universe, IOP Publishing, 2001, p. 327.
[11] A. Giorgilli, V. Lazutkin, C. Simó, Regular Chaotic Dynam. 2 (1997) 47.

[12] G. Gómez, J.M. Mondelo, C. Simó, Refined Fourier analysis: procedures, error estimates and applications, Preprint, 2002.
[13] K. Goździewski, E. Bois, A. Maciejewski, L. Kiseleva-Eggleton, Astron. Astrophys. 378 (2001) 569.
[14] K. Goździewski, A. Maciejewski, The Astrophys. J. 563 (2001) L81.
[15] K. Goździewski, E. Bois, A. Maciejewski, MNRAS 332 (2002) 839.
[16] I. Gradshteyn, I. Ryzhik, Table of Integrals, Series and Products, Academic Press, New York, 1980.
[17] E. Hairer, S. Nørsett, G. Wanner, Solving Ordinary Differential Equations. I. Nonstiff Problems, Springer, New York, 1987.
[18] M. Hénon, C. Heiles, AJ 69 (1964) 73.
[19] J. Laskar, Icarus 88 (1990) 266.
[20] J. Laskar, Physica D 67 (1993) 257.
[21] J. Laskar, in: C. Simó (Ed.), NATO–ASI Hamiltonian Systems with Three or More Degrees of Freedom, Kluwer Academic Publishers, Dordrecht, 1999, p. 134.
[22] L. Ledrappier, M. Shub, C. Simó, A. Wilkinson, Random versus deterministic exponents in a rich family of diffeomorphisms, J. Stat. Phys., to be published.
[23] Y. Papaphilippou, J. Laskar, Astron. Astrophys. 329 (1998) 451.
[24] P. Prince, J. Dormand, J. Comp. Appl. Math. 35 (1981) 67.
[25] C. Simó, in: H.W. Broer, B. Krauskopf, G. Vegter (Eds.), Global Analysis of Dynamical Systems, IOP Publishing, 2001, p. 263.
[26] C. Simó, Numerical indicators of the dynamics, Applications to diffusion, 2002, in preparation.
[27] C. Simó, C. Valls, Nonlinearity 14 (2001) 1707.
[28] M. Valluri, D. Merritt, ApJ 506 (1998) 686.